EFFECT OF SINGLE MODE INITIAL CONDITIONS IN RAYLEIGH-TAYLOR TURBULENT MIXING

A Thesis

by

YUVAL DORON

Submitted to the Office of Graduate Studies of
Texas A&M University
in partial fulfillment of the requirements for the degree of

MASTER OF SCIENCE

December 2009

Major Subject: Mechanical Engineering

EFFECT OF SINGLE MODE INITIAL CONDITIONS IN RAYLEIGH-TAYLOR TURBULENT MIXING

A Thesis

by

YUVAL DORON

Submitted to the Office of Graduate Studies of
Texas A&M University
in partial fulfillment of the requirements for the degree of

MASTER OF SCIENCE

Approved by:

Chair of Committee,	Andrew Duggleby
Committee Members,	Devesh Ranjan
	Kevin Krisciunas
Head of Department,	Dennis O'Neal

December 2009

Major Subject: Mechanical Engineering

ABSTRACT

Effect of Single Mode Initial Conditions in
Rayleigh-Taylor Turbulent Mixing. (December 2009)
Yuval Doron, B.S, University of Texas at Austin
Chair of Advisory Committee: Dr. Andrew Duggleby

The effect of single mode initial conditions at the interface of Rayleigh-Taylor (RT) mixing are experimentally examined utilizing the low Atwood number water channel facility at Texas A&M. The water channel convects two separated stratified flows and unifies them at the end of a splitter plate. The RT instability is attained by convecting a cold stream above a warmer stream. Average density calculations are based on long time average optical measurements. The water channel was modified with a flapper fin like device at the end of the splitter plate which was actuated by a computer controlled servo motor. Other modifications to the experiment were implemented resulting in reduced uncertainty. The experiment examined five different modes in addition to the baseline: 2 cm, 3 cm, 4 cm, 6 cm, and 8 cm wavelengths. The mixing width growth rates were shown to be dependent on initial conditions. Additionally, it appears that the growth rates commence with terminal velocity and are observed to line up with the baseline case.

To Dr. Philip S. Schmidt

ACKNOWLEDGMENTS

I would like to thank the Department of Mechanical Engineering at Texas A&M for providing the facilities in which the experiments were performed. In addition, I would like to thank Dr. Andrew Duggleby for his continued support and efforts to see this project through. I would like to thank Dr. Andrews for sponsoring this project and starting me on the experimental path for this research. I would like to thank my dear wife for allowing me to pursue this degree even though it meant little salary and many hours away from home.

TABLE OF CONTENTS

Page

LIST OF TABLES

LIST OF FIGURES

FIGURE Page

FIGURE Page

CHAPTER I

INTRODUCTION

A. Motivation

Out of the many studied phenomena in nature, turbulent flows remain unsolved. The complex behavior of turbulent flows with varying length scales is chaotic in nature, implying unpredictability. This prevents any model from completely describing all fluid particles at any instance in time and space. Turbulent flows stretch and fold the fluid in an endless cycle leading to efficient mixing, in an effort to homogenize the fluid.

Nature provides various methods that generate turbulent flows. For example, the energy provided to turbulent flows in water streams and rivers is the potential energy generated by the gravitational force of the Earth on the water. Energy for turbulence in oceans is provided by both lunar gravity on tide mobility, and the gravity effect on density gradients which are influenced by either salt concentrations or thermal gradients [1]. A density gradient in a fluid under a gravitational field, (i.e. earth) where the higher density fluid is supported by the lower density fluid was first studied by Lord Rayleigh and published in 1883 [2]. Einstein realized that gravity and acceleration are interchangeable, and in 1950 Taylor broadened the Rayleigh study to include a heavy fluid that is accelerated into a lighter fluid [3]. Thus the title now bears both their names and is known as the Rayleigh-Taylor hydrodynamic instability (RT). The RT instability has now been attributed to many natural occurring events to include supernovae, nebula fingers, oceanic and atmospheric instabilities, and salt dome formations.

The journal model is *IEEE Transactions on Automatic Control.*

In addition, the RT instability is partially responsible for the failure to attain a thermonuclear ignition in Inertial Confinement Fusion [4]. Inertial confinement fusion (ICF) is a process by which a spherical capsule composed of a solid Deuterium-Tritium (DT) shell is imploded utilizing laser surface ablation [5]. During the implosion process the ablated material forces the shell to accelerate inwards thus compressing the DT shell onto itself as represented in Figure1. The shell then reaches a stagnation

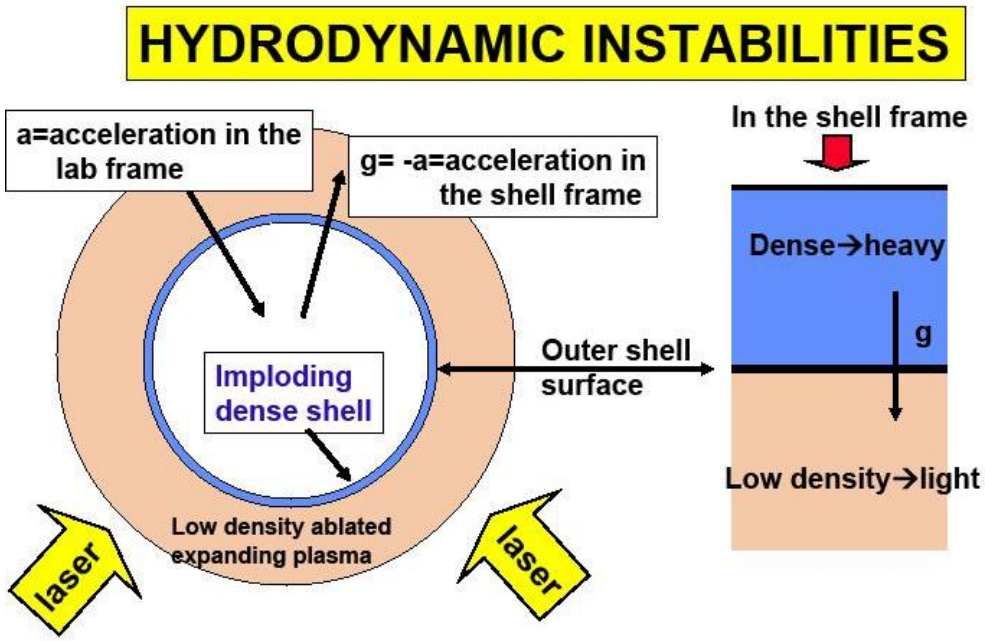

Fig. 1. An illustration representing the hydrodynamic instability in an imploding DT capsule. The capsule implodes and accelerates inwards, from the reference frame of the capsule, the heavy DT is accelerated outwards into the lighter expanding DT gas. An analogous example is a driver in an accelerating car, though the car is accelerating in the forward direction, the driver is accelerated against his seat.(Figure taken from Hydrodynamic Instability lecture presented at the HEDP 2009 UCLA summer school)

point where the remaining DT material forms a hotspot. If sufficient DT material remains in the hotspot, a thermonuclear ignition occurs. During the implosion process the surface of the DT shell decomposes into two separate states of matter. On the

ablated surface, expanding light density plasma is formed. The light density plasma encapsulates the denser imploding DT material. Choosing a reference frame at the interface between the light density plasma and the heavy DT material implies that denser material is accelerated into lighter material resulting in RT hydrodynamic instability as shown in figure 1. The instability has two main effects on the DT capsule: mixing between the two states of DT material (resulting in internal shell deformation), and shell rupture. The internal deformation may result in less than sufficient critical mass of DT material in the hotspot thus preventing ignition. The shell rupture prevents internal pressure to rise, (resulting in minimal temperature increase) thus limiting the formation of the hotspot.

Exploring the RT mixing characteristics to further understand its effects in ICF is therefore of interest to the scientific community. Understanding the instability growth rate process may help develop a means to limit RT effects in ICF thus paving the way towards nuclear fusion and thereby providing energy abundance. Its been suggested that altering RT initial conditions may result in different mixing width growth rates [6]. For the ICF community this could mean altering the DT capsule design with preexisting surface deformations, thus altering initial conditions. The subject of this thesis is to experimentally explore the effects of single mode perturbations at the interface of the heavy over light fluid in a low-Atwood number water channel through implementations of a flapping device.

B. Background

The RT instability manifests itself in the presence of gravity when

$$\nabla\rho \cdot \nabla P < 0, \tag{1.1}$$

under this unstable condition mixing will occur by any slight system perturbation. Due to natural noise, a perturbation is induced at the interface and thus initiates the instability. Once the instability is initiated a vorticity is generated along the interface, known as the baroclinic vorticity. The baroclinic vorticity equation is derived by taking the curl of the pressure gradient in the Navier-Stokes equation,

$$\nabla \times \left(\frac{-1}{\rho} \nabla \rho \right) = \nabla P \times \frac{\nabla \rho}{\rho^2} \tag{1.2}$$

and is nonzero when the pressure and density gradients are misaligned [7]. The vorticity helps to drive the instability further away from equilibrium which then leads to the formation of the familiar "bubble" and "spike" structures. Where the bubble refers to the rising lower density fluid, and the spike refers to the sinking higher density fluid as shown in Figure 2. The buoyancy forces acting on the lower density

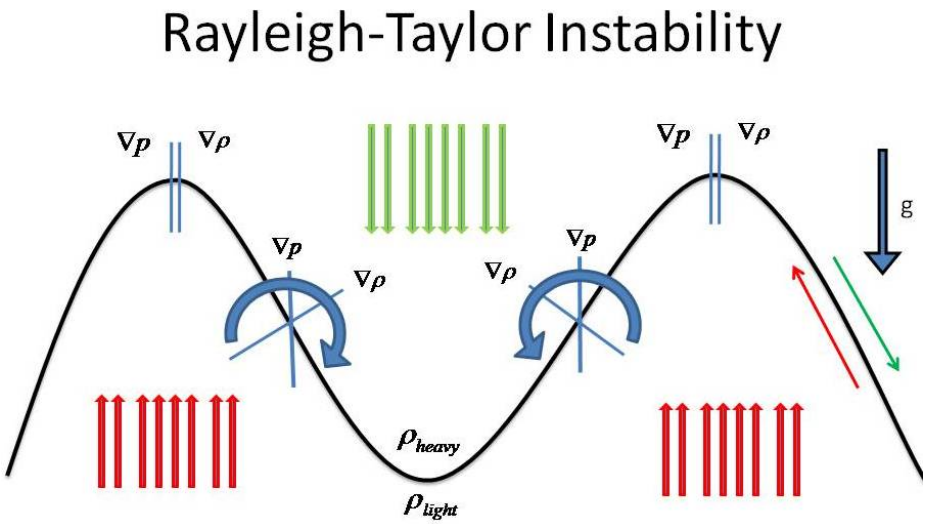

Fig. 2. Qualitative meaning of the RT instability. The baroclinic vorticity is shown to be zero on the peak and valley of the sinusoidal interface where the pressure gradient and density gradients are aligned, but is non-zero at the crests.

fluid and forcing it upwards are generated from the gravitational forces acting on the heavy fluid. As the bubble and spike formations move in opposite directions they

generate vortices along the interface which increase the surface area between the two fluids, inducing further mixing. This condition is known as the Kelvin-Helmholtz instability and is responsible for the mushroom, like features present in the bubble and spike formations.

An additional parameter that helps characterize the growth rate in the RT instability is the Atwood number:

$$A_t = \frac{\rho_1 - \rho_2}{\rho_1 + \rho_2} \tag{1.3}$$

where $\rho_1 > \rho_2$. The Atwood number (A_t), indicates if the bubble and spike structures will grow in a symmetrical or asymmetrical manner [8]. The two limits on the A_t number are zero and asymptotic to one. Zero indicates that $\rho_1 = \rho_2$, and thus the instability does not exist. An A_t number of one which is un-physical, indicates that ρ_1 is infinitely larger than ρ_2. Through experimentation it has been observed that for a small A_t number the RT instability will behave in a symmetrical fashion. This means that the bubble and spike formation will grow equally in opposing directions. However, as the A_t number increases, the symmetrical nature of the instability decreases. In ICF the A_t number is on the order of 0.9, indicating that the RT instability behaves in an asymmetrical manner, resulting in a larger growing spike than a bubble [5]. Whereas the A_t number in water instabilities for the water channel at Texas A&M is on the order of 10^{-4}, indicating the instability behaves in a more symmetrical nature.

1. Temporal Evolution of Rayleigh-Taylor Mixing

Since the first study of the RT instability in 1883, a complete model describing the instability remains elusive due in part to the complex modes that exist and vary as the instability grows. Over the last 25 years the temporal evolution of the mixing

width has been characterized into three regimes [9]:

1. **Exponential Growth**, where any perturbation grows exponentially.

2. **Mode Coupling** growth rate slows to become non-linear, large structures appear, memory of initial conditions begin to subside.

3. **Similarity**; viscosity effects are negligible on the growth rate, and the mixing is described by a similarity solution proportional to gt^2.

The mixing width, or mixing height is defined as:

$$h = \frac{(h_b - h_s)}{2} \tag{1.4}$$

where h_b is the point where the average non-dimensional density is

$$\overline{f}_1 = \frac{(\overline{\rho} - \rho_2)}{(\rho_1 - \rho_2)} = 0.95 \tag{1.5}$$

and h_s is

$$\overline{f}_1 = 0.05 \tag{1.6}$$

The first of these three regimes is based on the most unstable wavelength as described by Chandrasekhar [10], and is written as:

$$\lambda_m \approx 4\pi \left\{ \frac{\nu^2}{g} \frac{1}{A_t} \right\}^{\frac{1}{3}} \tag{1.7}$$

The second regime characterizes the evolution of large structures that arise from the non-linear interactions of smaller structures and not necessarily from initial conditions. The evolution of large structures as previously mentioned is a combination of the bubble and spike formations and from the second Kelvin-Helmholtz shear instability. These structures will grow until they reach terminal velocity based upon their size [11]. The point at which terminal velocity is achieved is known as saturation,

and the fully developed structures appear. From this point forward the transition to turbulence begins. The third regime is denoted by similarity, and is defined by the structures growing to infinity. This condition can only occur if the system size $H >> h$, which permits the Reynolds number to go to infinity. The Reynolds number is characterized by the bubble and spike structures:

$$Re = \frac{\dot{h} \cdot h}{\nu}. \tag{1.8}$$

where h is the mixing height characterized by $\overline{f}_1$, and $\dot{h}$ is the growth rate of the mixing height. Then, if Re $\rightarrow \infty$ and initial conditions are indeed lost due to chaos, self-similarity exists. Youngs arrived at the equation describing the mixing height growth based on these three regimes. The equation states that $h = \alpha A_t g t^2$ where $\alpha = \frac{2\pi}{N^2}$ and $N^2 = n_m t$. For the past 25 years α has been sought after by the RT scientific community, where $0.03 < \alpha < 0.07$. However, this equation is based on the assumptions that viscosity is zero, which is not physical. Additionally, Youngs assumed that the system size is infinitely larger than the instability growth structures, which is never the case. Thirdly, Youngs assumed that initial conditions are lost. However, recent experiments and simulations by Dimonte [6], Ramaprabhu [12], and Olson [13] show late-time dependence on the initial perturbation of the fluid interface. This implies that the third similarity assumption of memory loss of initial conditions has not yet occurred. These results are significant as they pave the way towards experimentation of initial conditions at the interface. The author and his advisor, contend that α does not exist. The conclusion is based on the un-physical assumptions suggested by Youngs which resulted in the gt^2 through dimensional analysis as the only remaining length scale, thus ignoring other possible turbulent length scales. The author and his advisor believe the instability growth is a function of other turbulence length scales yet to be identified.

2. Previous Experiments

In the past 25 years there have been many attempts to simulate experimentally the RT instability. Some experiments focus on the basic nature of the instability while some attempt to simulate specific RT instabilities such as in the ICF implosion process. The basic premise for conducting RT experiments involves the following:

1. Identifying the A_t number regime to be used.
2. Choosing the method of varying the density in the medium in order to achieve the sought after A_t number.
3. Choosing a process where a stratified heavy fluid over light fluid can be controlled and perturbed.
4. Choosing data capturing diagnostics.
5. Evaluating combined associated uncertainty for the process and diagnostics.
6. Evaluating cost of experiment.

The following are examples of RT experiments that focused on the basic nature of RT instability. In 1984, Reid designed a rocket rig that accelerated two stratified fluids to 75 g, thus initiating the RT instability [14]. The experiment is expensive in its nature to operate and offers little time for capturing data. In 1990, Andrews and Spalding designed an experiment for RT instability by inverting a device which contained two fluids with different densities [15]. The device held two fluids in between two clear walls. The device was able to rotate on its axis with one degree of freedom. The two fluids were stratified with the heavy fluids below the light, and thus creating a stable system. The experiment commenced when the device was rapidly inverted to initiate the instability. The experiment was not costly to operate and used photography for

data acquisition. Similar to Read's rocket design, in 1996, Diomonte and Schneider designed a rig that used magnetic motors instead of the rockets to accelerate the device [16]. In 1994, Andrews and Snider developed an experiment that utilized a water channel that convected two initially separated stratified flows of heavy over light fluid. The densities were varied by temperature with the difference of approximately 5 degrees Centigrade [17]. This experiment is relatively cheap to operate, can offer over 20 minutes of data acquisition and optically measure density variation. The work compiled in this thesis was performed on a modified version of Snider Andrews water channel, and therefore the water channel experiment will be discussed in much grater detail throughout the body of this thesis.

3. Texas A&M Water Channel Facility

As mentioned in the previous section, the Texas A&M water channel facility was first conceived and designed in 1994. This was a novel design, and for the first time provided the RT community the opportunity to study the instability growth over a long evolutionary time. Since then multiple experiments were performed utilizing the channel, and with each experiment came modifications. The original design utilized two 540 liter water tanks and associated water pumps. The test section was build using plexiglass, and consisted of an inlet plenum and exit plenum. The two water tanks were filled with warm and room temperature water, respectively, thus generating the RT instability. The channel design provided multiple methodologies of data acquisition which included the following:

- Utilizing multiple thermocouple in the flow to measure density fluctuation.
- Optical measurement of density utilizing a back lit diffused light source with a camera.

- Planar laser induced fluorescent.
- Particle image velocimetry.
- Molecular mixing utilizing chemical reactions in the flow.

In 1997, Kieth Leicht designed a flapper experiment utilizing a thin plate at the end of the splitter plate. The flapper was controlled with a permanent magnet dc motor mounted on a rocking platform. The exact RPM of the motor was unknown which meant that Leicht was unable to quantify the effects on RT mixing width since the exact amplitude and frequency were unattainable. However, Leicht experiment paved the way for future work when more precise equipment became available [18].

4. Current Research Objectives

The current research described in the next few chapters of thesis came about as a result of the ICF scientific community interest to understand initial conditions in hydrodynamic instability [5], and by previous research performed by Keith Leicht. The research in its fundamental paradigm was to design a system that could be integrated into the current water channel at Texas A&M and perturb the RT interface in its infancy. The following are the objectives set for this research:

- Design a flapper at the end of the splitter plate to perturb the flow.
- Study the effects of single wavelength initial conditions on RT mixing.

After researching the previous experiment performed by Leicht and its shortcomings, the following constraints were set for this research:

- The Flapper must be manufactured with great precision to include a fine and flat knife edge.

- The system linkages that connected the motor to the flapper must be manufactured with similar precision as the flapper.
- The system of linkages must be limited in motion to one degree of freedom.
- The motor to operate the flapper must be computer controlled with a feedback system.

The reasoning for each one of the constraints will be thoroughly discussed in Chapter two of this thesis. Subsequent to the onset of the research additional shortcomings of the experiment were identified resulting in further channel modifications. Though these modifications were not set as the original objectives, implementing them resulted with a decrease in experimental data uncertainty. The modifications will be discussed throughout Chapter II.

CHAPTER II

EXPERIMENTAL SETUP

A. Experimental Methods

This section describes the low-Atwood number water channel facility at Texas A&M and the modifications thereof that enabled the implementation of controlled initial conditions downstream of the splitter plate at the flow interface.

1. Water Channel Description

The water channel is constructed out of plexiglass and provides a test section which is 50 inch long, $12\frac{1}{2}$ inches tall by 8 inches wide as shown in Figure 3 (Top). The channel is partitioned along the horizontal axis into top and bottom sections utilizing a splitter plate. Water from two separated 500 gallon tanks is pumped through individual pumps into the channel via an inlet plenum. The inlet plenum is exposed to atmospheric pressure and directs the water to the top and bottom sections of the channel respectively. Flow laminators composed of an array of 5 mm diameter by 20 cm long straws are installed past the inlet plenum and prior to the flapper in order to minimize free stream turbulence in the test section of the channel. The flow exits through an exit plenum which is also exposed to atmospheric pressure. The exit plenum's outflow is set to ensure a continuous streakline through the test section. Utilizing an Eulerian frame of reference distance downstream translates to time through $t = x/U$, where x indicates the axial distance downstream in the channel, and U is the uniform convective velocity.

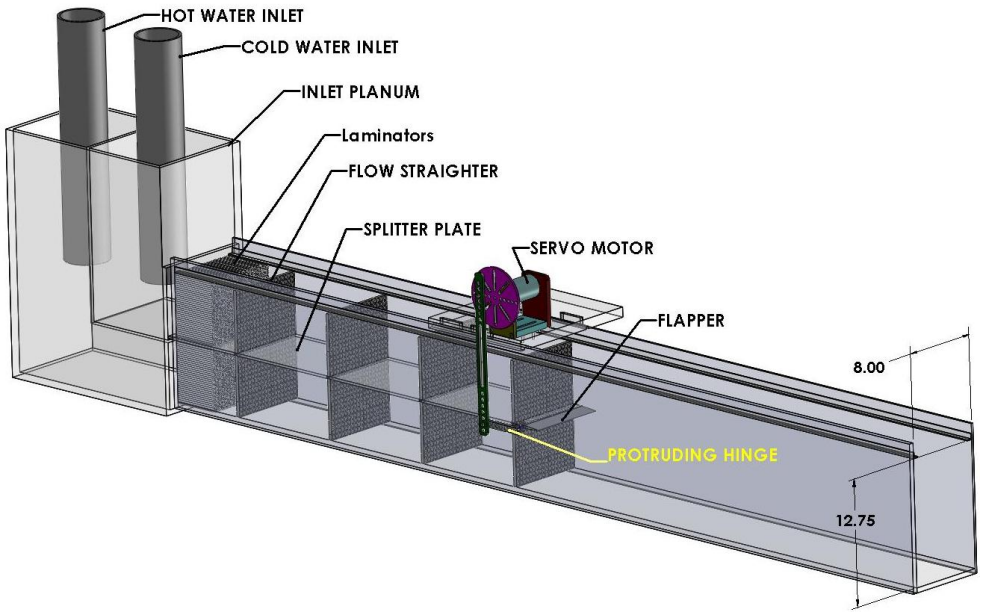

(a) Water channel main set up (Units are in inches)

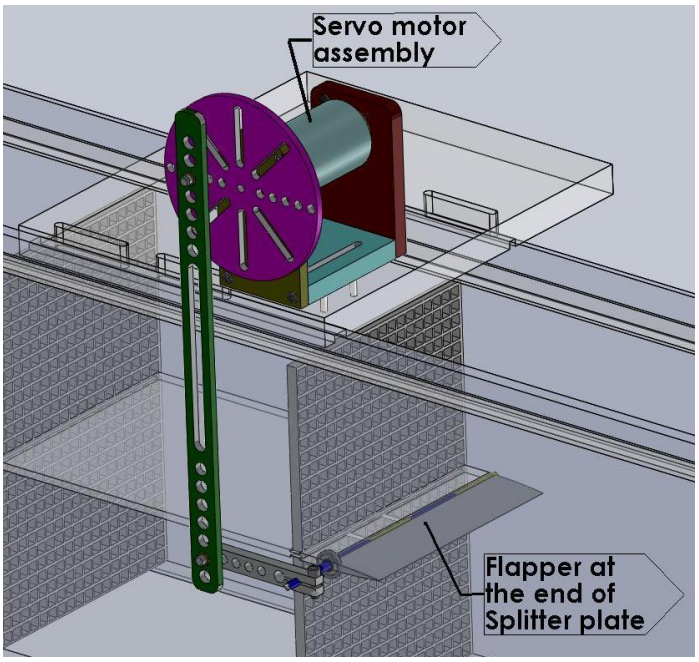

(b) Servo motor placement in the channel

Fig. 3. Figure (top) showing the water channel configuration. (bottom) Showing the servo motor assembly and attachment to the channel

2. Velocity Measurements

It is imperative that the flow in the top and bottom sections have equal velocity. If this condition is not met prior to running the experiment, then the Kelvin-Helmholtz shear instability will exist prior to the bubble and spike formation, thus complicating the analysis. In previous experiments the velocity of the top and bottom streams was matched utilizing two methods. The first method made use of a dual dye injection device, such that dye blobs were injected simultaneously to the top and bottom streams through two outlets while running the channel. By visually inspecting the dye blobs as they convected downstream, adjustments were made to the flow control valves for the top and bottom streams respectively until the blobs were matched in velocity. The second method was performed in order to measure the convective velocity in the channel test section. This was performed by placing two objects against the outside test section plexiglass wall, and injecting dye blobs into the convective flow. Using a stop watch and by visual inspection, the operator measured the time duration it took the dye blob to traverse between the two objects on the outside. This was performed repeatedly for approximately 10 times. The distance between the two objects was measured, and then divided by the time average.

This method was deemed to contain too large of uncertainty due to the large scatter of the time measurements. Therefore, a new approach was conceived to measure the velocity more accurately and minimize uncertainty while simultaneously ensuring equal flows of the top and bottom streams. In this new approach dye is injected into the top and bottom streams and photographed at 1 ± 0.005 second intervals, and the distance traveled by the dye between successive frames is converted from pixels to distance through a reference photograph of a ruler. This procedure is repeated until the velocities are matched using the inlet flow valves. Figure 4 shows a successive

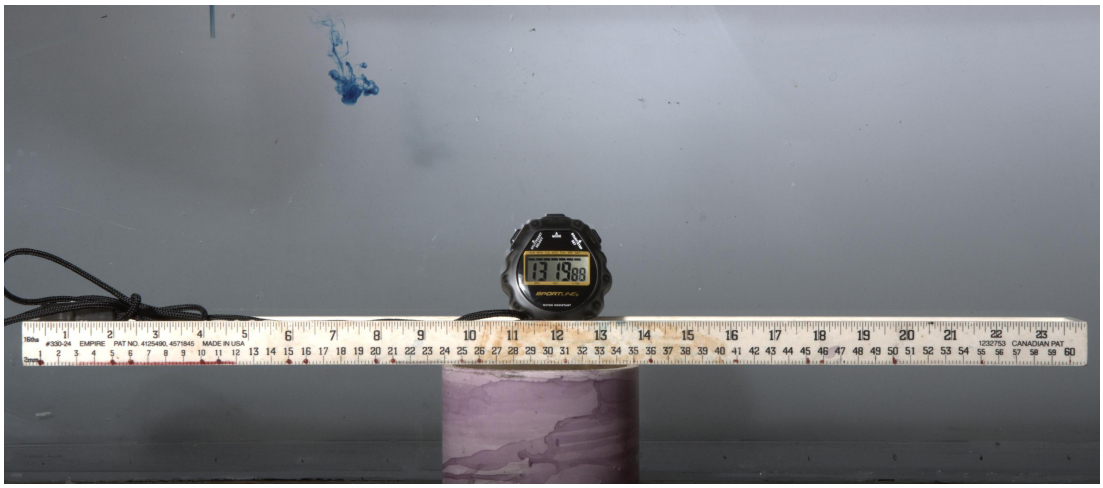

(a) Initial frame showing the dye blob in the flow

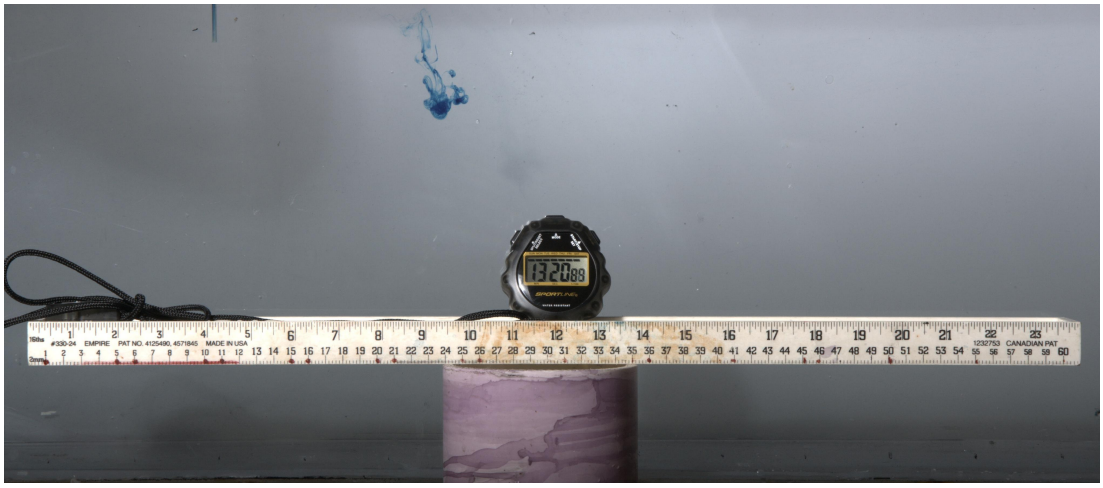

(b) Second frame showing the traversed dye blob

Fig. 4. Figure showing velocity measurements utilizing two consecutive photographs of dye blob in the flow. Notice the stop watch seconds and hundreds of a second, the interval time between both photographs is precisely one second $\pm$ 0.005 seconds.

set of photographs with the dye blob in the flow. The velocity uncertainty using a

Klein-McKlintock uncertainty analysis is:

$$dU = \sqrt{\left(\frac{dL}{t}\right)^2 + \left(\frac{(dt)L}{t^2}\right)^2}, \tag{2.1}$$

where dL is the length of associated with one pixel (around 0.25 mm) and dt is the uncertainty in the camera time (0.005 s) for error of approximately 0.5 % at typical operational velocities of 6 cm/s. Furthermore, applying a 2-D Reynolds Averaged Navier Stokes analysis, the velocity must be greater than 5 cm/s to ensure that the downstream turbulent mixing motions have only a negligible effect on the upstream motion.

The experiment was conducted with a low Atwood number on the order of 10^{-3} which is attained by a slight temperature difference between the top and bottom flows in the channel (5.0 °C higher on the bottom). Water samples are drawn from both the cold and hot water tanks and analyzed with the use of a densitometer. The Atwood uncertainty is

$$\frac{dA}{A} = \frac{1}{\rho_1 - \rho_2}\sqrt{((1-A)d\rho_1)^2 + ((1+A)d\rho_2)^2}, \tag{2.2}$$

where $d\rho_1 = d\rho_2 = 0.00005$ g/cm^3 using a densitometer from Rudolph, Inc. yielding density uncertainties of approximately 0.005% and an Atwood uncertainty of $dA/A \sim 4\%$.

3. Flapper Modification

A hinged foil was added to the channel at the end of the splitter plate, known as the flapper. The flapper spans the width of the channel with a negligible gap between channel walls and flapper. The flapper is 2 inches long and 0.25 inches thick at its thickest point located at the hinge section as shown in Figure 5. The flapper tapers off to a 0.006 inch knife edge with a 16.454 inch radius of curvature and 3.6 degrees

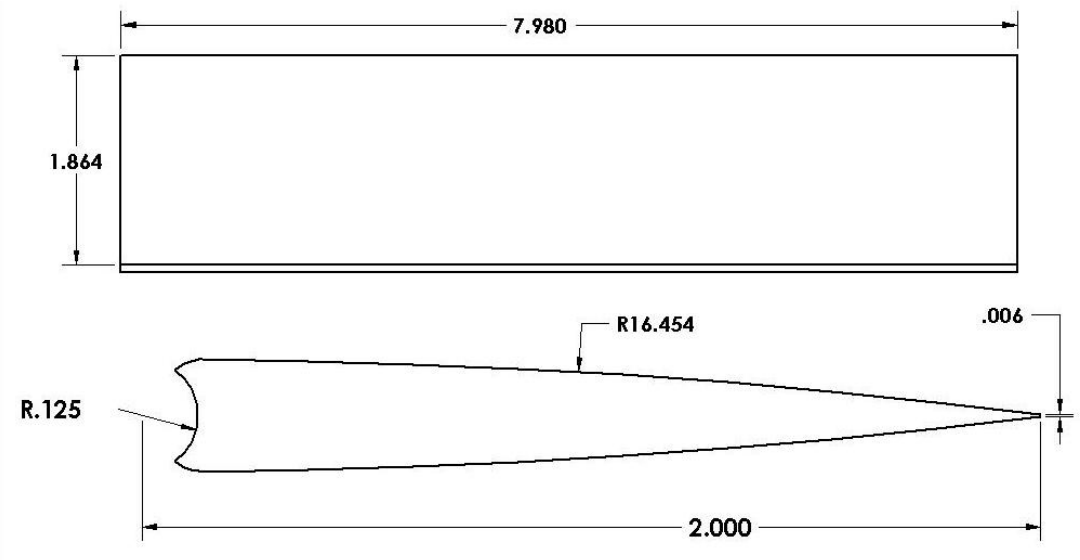

Fig. 5. Dimensions of the flapper installed at the end of the splitter plate. The 3.6° angle is sufficiently small to avoid any separation.

slope, which is sufficiently small to prevent flow separation over the flapper according to a triple deck boundary layer analysis [19]. The hinge design is based on a piano style hinge and provides a smooth transition between the splitter plate and the flapper to reduce possible flow disturbances. Aluminum was chosen for the flapper material to ensure minimal deflection of the flapper from the flow while in operation. The aluminum flapper was manufactured utilizing Computer Numeric Control Electrical Discharge Machining. This type of manufacturing ensures that minimal deformation occurs during the cutting process thus maintaining high tolerances.

At one end of the flapper, part of the welded hinge is extended 2 inches past the channel width and protrudes through the channel side wall as shown in Figure 6. A shaft seal serves to minimize any leakage out of the channel. A system of linkages connects the extended portion of the hinge to a servo motor as shown in Figure 3 (bottom). The linkages are connected to one another with high precision bushing and bearing surfaces, thus providing motion with only one degree of freedom. The

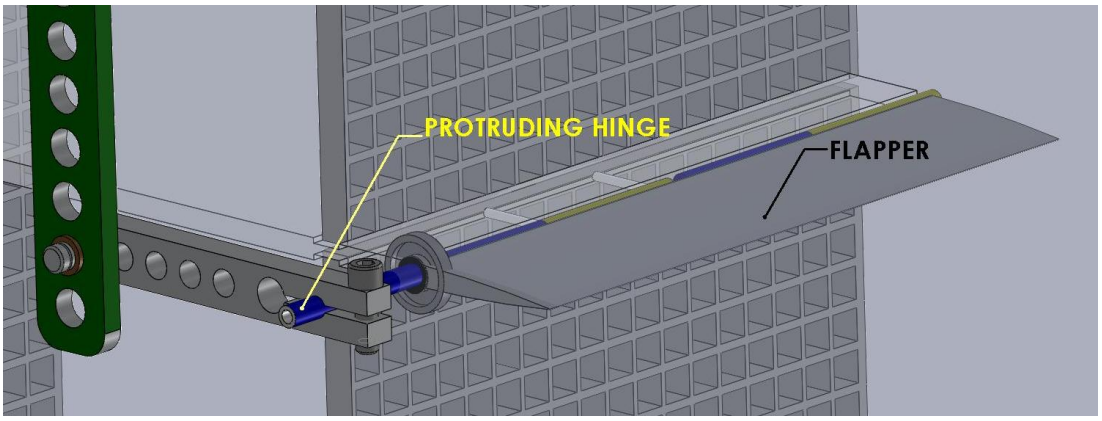

Fig. 6. Flapper design shows the hinge protruding through the channel wall. The hinge is welded to the flapper and connects to the lineages via securing clamp.

servo motor is securely mounted to the top of the channel and is controlled via motion controller from Galil Tools which is connected to a laptop. The motor's servo provides 4000 counts per revolution which yields a high degree of motion control. The servo system is a closed loop feedback system thus ensuring correct motor shaft position at all times. The linkage system allows the flapper to oscillate with controlled frequency and amplitude. A later section will discuss the flapper oscillations in further detail.

4. Vibration Analysis

Steps were taken to reduce natural system noise and verify that the water channel operates "quietly" with no free-stream turbulence. As described previously, water is pumped into the channel via piping through individual pumps. Each pump provides an average flow rate of 30 gpm which passes through $1\frac{1}{2}$ inch pipe and transitions to 4 inch pipe prior to entering the channel. Up to the current research, the inlet pipes were secured to the channel by a wood frame. Induced vibrations from the water pumps and water traversing through the pipes were directly transferred to the water channel. It was the wish of the author to minimize any unnecessary noise from

Fig. 7. In order to minimize any sources of vibrations to the channel, the water inlet pipes were detached from the channel and suspended above the inlet plenum, such that no physical contact exists between the channel and water pipes.

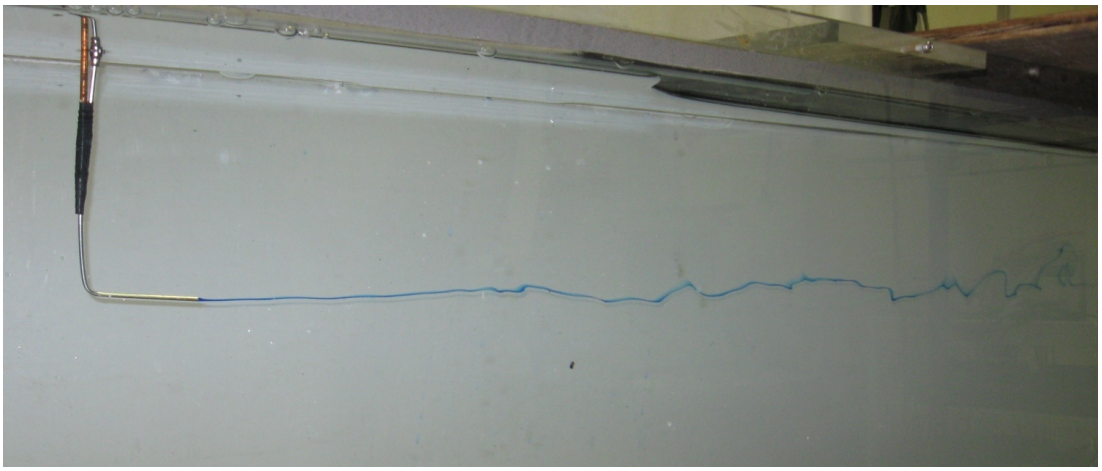

Fig. 8. Streakline is shown in the top section of the channel. The streakline is generated with a dye through a fine needle placed in the flow. The flow rate of the dye is set to match the velocity of the free-stream to avoid disrupting the flow and thus ensuring accurate flow visualization. The long coherent streakline is evidence that the flow in the channel has no free-stream turbulence. Any free-stream turbulence would quickly mix and dissipate the streak.

the channel. Thus, in order to reduce any possible vibrations from the pipes to the channel, straps were secured to the ceiling and used to suspend the pipes above the inlet plenum in such a manner that no physical contact exists between the pipes and the channel as shown in Figure 7.

Thus, the only vibrations in the channel are natural system vibrations caused by the flowing water in the channel and the oscillating flapper. The channel was monitored while in operation with the oscillating flapper utilizing an accelerometer. The readings showed that the natural noise of the system was one tenth of that of the oscillating flapper. The streakline shown in Figure 8 is evidence that minimal flow disturbances and no free-stream turbulence exists in the channel. If free-stream turbulence were present, this streakline would quickly be mixed and dissipated.

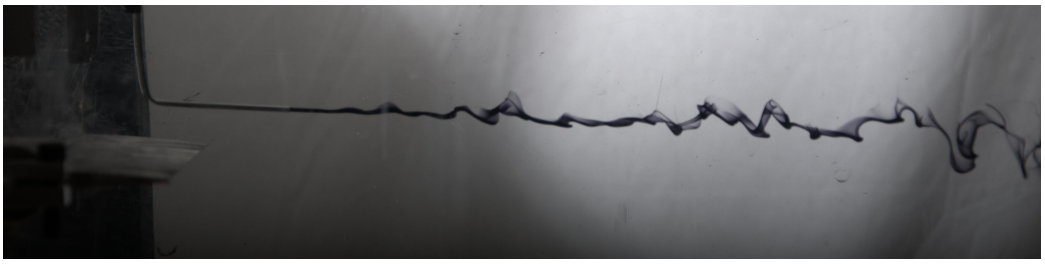

(a) Initial frame showing the dye stream exiting the needle.

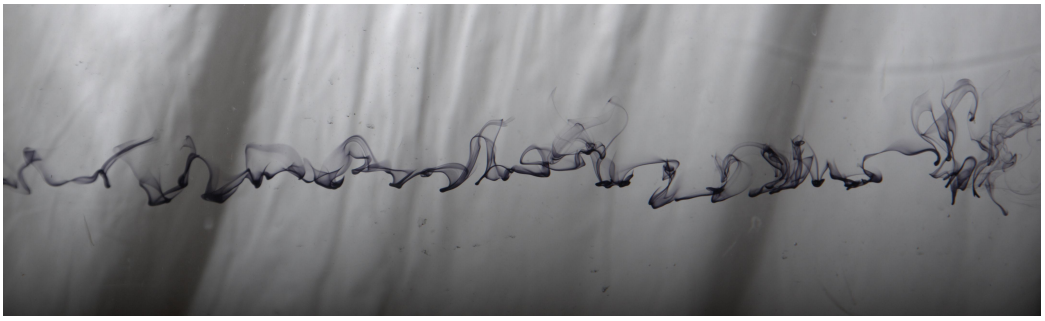

(b) Second frame showing the traversed dye stream breaking up.

(c) Third frame showing the traversed dye stream more condensed as it enters the exit plenum.

Fig. 9. Figure showing dye exiting needle, as the dye streak continues downstream it is observed to break up. Close to the end of the channel test section the streak is broken up but appears to be more uniform as it enters the exit plenum.

5. Controlling Free-stream Turbulence

Controlling free-stream turbulence presented itself as an unsolvable issue for this channel. The previous section makes note that of the controlled vibration and the

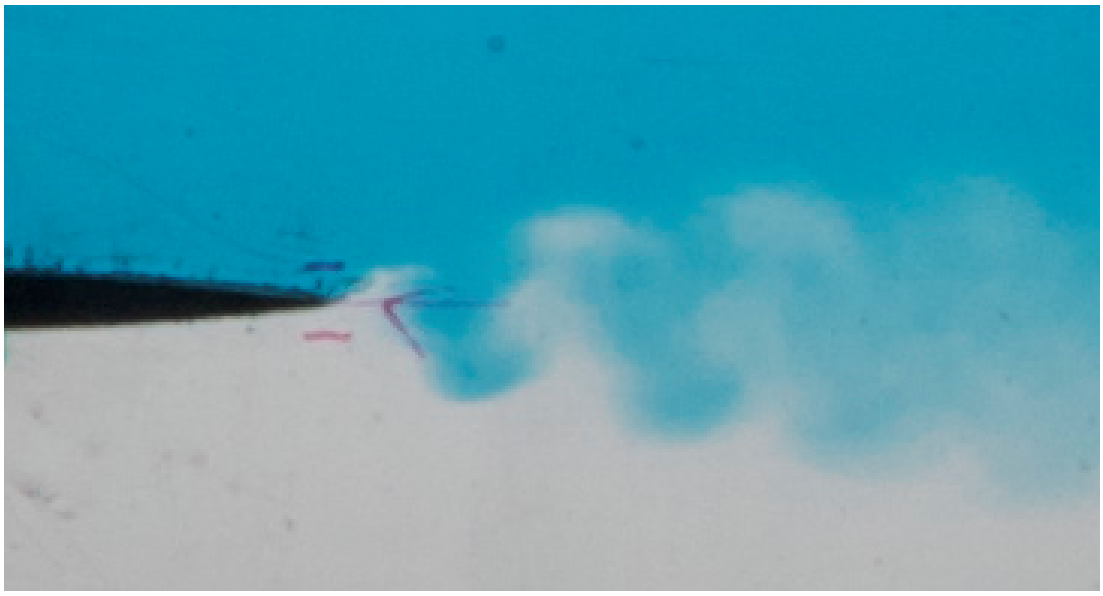

Fig. 10. Severe leaning observed on the spike and bubble formation due to boundary layer development of the flapper.

unbroken streakline in the test section. However, due to the velocity profiles exiting the flow laminators a decision was made to move them upstream. Placing the laminators further upstream meant that flow straighteners were placed in close proximity to the flapper. This method removes large eddies from the flow test section but free-stream turbulence was observed in the middle region of the test section as shown in Figure 9. Not placing the flow straighteners close to the flapper yielded a large boundary layer at the end of the flapper. The boundary layer coming off the flapper caused sever leaning on the bubble and spike formations as shown in Figure 10.

6. Flapper Oscillations

The main change and difference between this experimental set up and that of Keith Leicht, is the flapper design and set up. In contrast to Leicht's flapper which was manufactured from a thin and flexible plate and held by a single $\frac{1}{8}$ inch rod set in the middle of the flow, and controlled by two DC permanent magnet motors. The new

(a) Large vortex formation &shedding

(b) Multiple vortex shedding

Fig. 11. If the amplitude of the flapper is on the same order of magnitude as the convective velocity, then a non-negligible vortex shedding will occur off the flapper.

flapper was rigid, precise, and controlled by a servo motor with a feedback system. The linkages were placed on the outside of the channel, so as to not disrupt the flow in the test section. The linkages and servo motor were designed in a manner that would simplify the dynamic calculations. Vortex shedding off the flapper was

observed if the frequency and amplitude were high as shown in Figure 11. This condition occurs when the flapper generates a vortex at the the tip, by oscillating too quickly. Realizing this meant that the amplitude and frequency must be dependent on the desired wavelength (λ), and convective flow velocity U_m. Utilizing a simple set of dynamic equations the flapper oscillations were then solved with an equation solver program. The calculations were based on the amplitude and frequency desired for the flapper motion. Figure 12 shows the sketch used to identify parameters for the dynamic calculation.

Starting with the geometry of the linkages, L_m which is the distance from the center of motor shaft to the center location of the vertical arm. L_f is the length of the flapper from tip to center of rotation. And L_A is the distance from flapper point of rotation to vertical arm point of connection. Using a relationship of the motor rotation to the flapper oscilation yields:

$$\theta_f = \arcsin\left[\left(\frac{L_m}{L_A}\right)\cdot\sin\theta_m\right] \tag{2.3}$$

Next solving for the flapper amplitude (d_f) at the tip in terms of the θ_f, and only considering motion for half the channel yields:

$$d_f = L_f \sin\theta_f \tag{2.4}$$

Since the servo motor uses 4000 counts per revolution, the motor rotation is related by:

$$\theta_m = Mtr_{counts}\cdot\left(\frac{360}{4000}\right) \tag{2.5}$$

As previously stated the frequency of the flapper is dependent on the convective velocity (U_m) and wavelength (λ) desired. However, since the servo motor operates

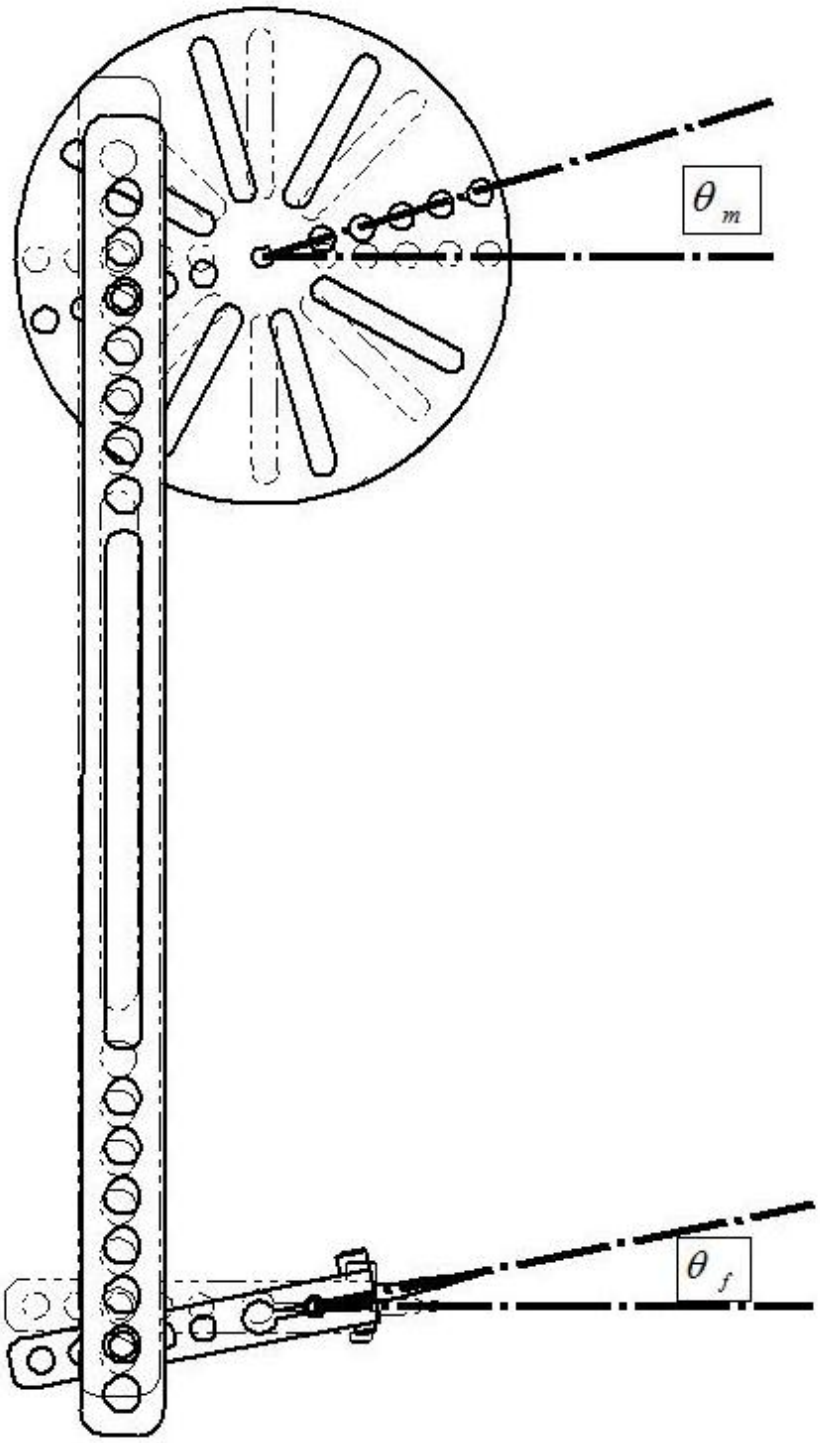

Fig. 12. Figure shows the sketch that was used to identify parameters for dynamic calculation. Where θ_m is the amount of rotation for the motor, and θ_f is the rotation for the flapper. And d_f is the amplitude in mm of the flapper.

with time dependency in order to generate a sin function for the perturbation, then:

$$Time = \left(\frac{\lambda}{U_m}\right), \tag{2.6}$$

and flapper amplitude becomes

$$Flpr_{amp} = \left(\frac{Time \cdot 0.65 \cdot U_m}{2\pi}\right). \tag{2.7}$$

Where 0.65 is the factor controlling the maximum vertical tip velocity of the flapper relative to the convective flow. Table I shows a sample outputs based on the convective flow velocity (U_m) and wavelength (λ) desired.

Table I. Table showing calculations performed to solve for flapper amplitude and frequency. The calculation is based on the desired flapper amplitude and convective flow velocity. The outputs of the calculation are then inputed to the servo computer control program.

Run	motor	time (ms)	Flapper amplitude (mm)	θ motor	θ flapper	λ	U_m
1	5.00	350.9	0.2069	0.4501	0.2334	2	5.7
2	7.501	526.3	0.3104	0.6751	0.35	3	5.7
3	10	701.8	0.4138	0.9001	0.4667	4	5.7
4	15	1053	0.6207	1.35	0.7001	6	5.7
5	20.01	1404	0.8276	1.8	0.9335	8	5.7

7. Data Acquisition

The water channel operation provides approximately 20 minutes of data acquisition time. The data acquisition is performed with a Nikon D90 digital camera. Light from a pair of strategically located flashes impinges on a diffusion sheet placed behind the channel. It is this light that passes through the channel and into the camera. To

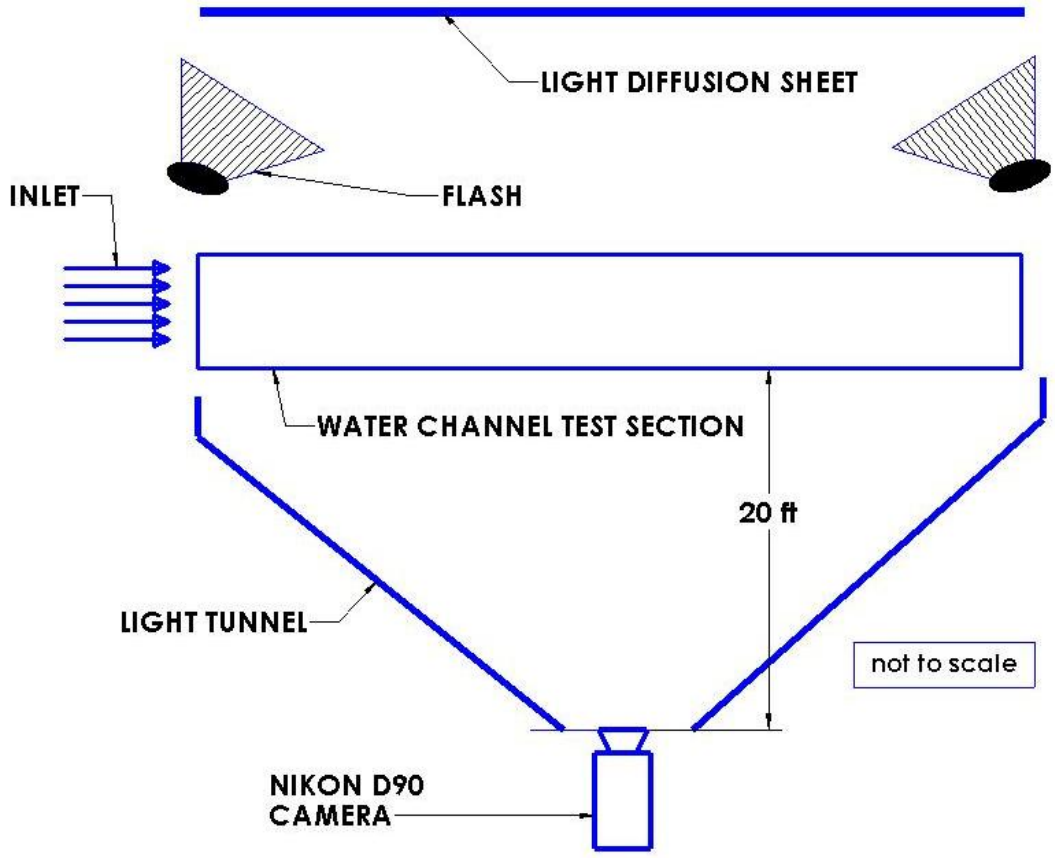

Fig. 13. Top view illustration of camera placement and flashes. The light emanating from the flashes impinges on the diffusion sheet behind the channel, travels through the experiment, and is recorded in the digital camera.

ensure that no other light source is captured by the camera except the light going through the channel, and to prevent stray light reflections from illuminating the experiment, a black tarp like material is set as a tunnel between the camera and the channel. To reduce error from parallax to acceptable levels, the camera is placed 20 ft away from the channel, Figure 13 shows the top view of this arrangement. To ensure no additional optical errors, circle of confusion (c) of the camera is set to one pixel. For the Nikon D90 with a sensor size of 23.6 mm, $c = 5.5\mu$m. The depth of

field (DOF) of the image is based on the camera lens focal length F and aperture size F/N.

$$\text{DOF} = zF^2\left(\frac{1}{F^2 - Nc(z-F)} - \frac{1}{f^2 + Nc(z-F)}\right). \tag{2.8}$$

With a focal length of $F = 105$ mm and aperture setting of $N = 16$, DOF = 371 mm (14.6 inches) which more than covers the entire width of the channel. With the resolution of 4288 x 2848, the one pixel spans 0.25 mm of the experiment. At a convective velocity of U=5.7 cm/s, the exposure time is set to 1/320 s with studio flash duration of 1/1200 s to ensure no blurring. This combination of small aperture and quick exposure time required the installation of studio flashes to provide the adequate backlight intensity to maintain the high quality image (ISO 200) on the Nikon D90.

8. Density Measurements

Density measurements through the span of the test section are obtained optically through the use of the Beer-Lamberts law. This law relates the spanwise gradient in light intensity I to the molecular absorbtion ϵ and concentration C:

$$\frac{\partial I}{\partial z} = -\epsilon C I, \tag{2.9}$$

as long as the solute is purely absorptive (no scattering) and the light is monochromatic and parallel. To ensure this, Nigrosine dye is used as a solute for its good absorptivity characteristics (negligible scattering). Additionally, the light off the white diffusive screen is nearly parallel into the camera at a distance of 20 ft. Finally, only the red channel in the digital camera is used to ensure monochromatic light, as the Nigrosine has a slightly scatters blue light (not purely black). Integrating equation

2.9 across the span of water channel w yields:

$$\ln \frac{I}{I_0} = -\epsilon w \overline{C}. \tag{2.10}$$

where I_0 is the light intensity through the water channel with clear water, I is the remaining light intensity for a given photograph passing through the experiment and $\overline{C}$ is the spanwise averaged concentration. Note that this equation only holds for a constant ϵ. If the dye concentration is too high, ϵ will not be constant. This constraint is tested by measuring the absorption through a triangular wedge filled with the diluted Nigrosine mixture. As seen in Figure 14 the absorption increases linearly with the width of the wedge so ϵ is constant. Because the Schmidt number of the Nigrosine is larger than the Prandtl number of the water, the motion of the Nigrosine is slaved to the fluid motion and the thermal mixing. Therefore, a measurement of Nigrosine concentration is associated with a density ρ, with $\rho_2 < \rho < \rho_1$ and ρ_1 and ρ_2 are the initial densities for the top and bottom channels, respectively. The average density $\overline{f}_1$ is obtained by averaging over many samples (500 photographs). The uncertainty of the mixing height dh has two sources, an uncertainty in y from the parallax of the camera (dy), and an uncertainty due to resolving the location of $\overline{f}_1 = 0.95$:

$$\frac{dh}{h} = \sqrt{\left(\frac{dy}{h}\right)^2 + \left(\frac{d\overline{f}_1}{h}\left(\frac{\partial \overline{f}_1}{\partial y}\bigg|_{\overline{f}=0.95}\right)^{-1}\right)^2}. \tag{2.11}$$

Here the low-Atwood symmetry is applied such that $h = y_{\overline{f}_1=0.95}$. $\overline{f}_1$ is rearranged using the property of the natural log:

$$\overline{f} = \frac{1}{N\epsilon L}\sum_{n=0}^{N} \ln\left(\frac{I(t_n)}{I_0}\right) = \frac{1}{N\epsilon L} \ln\left(\prod_{n=0}^{N} \frac{I(t_n)}{I_0}\right) \tag{2.12}$$

where $I(t_n)$ is the measured intensity at sample time t_n, L is the distance the light

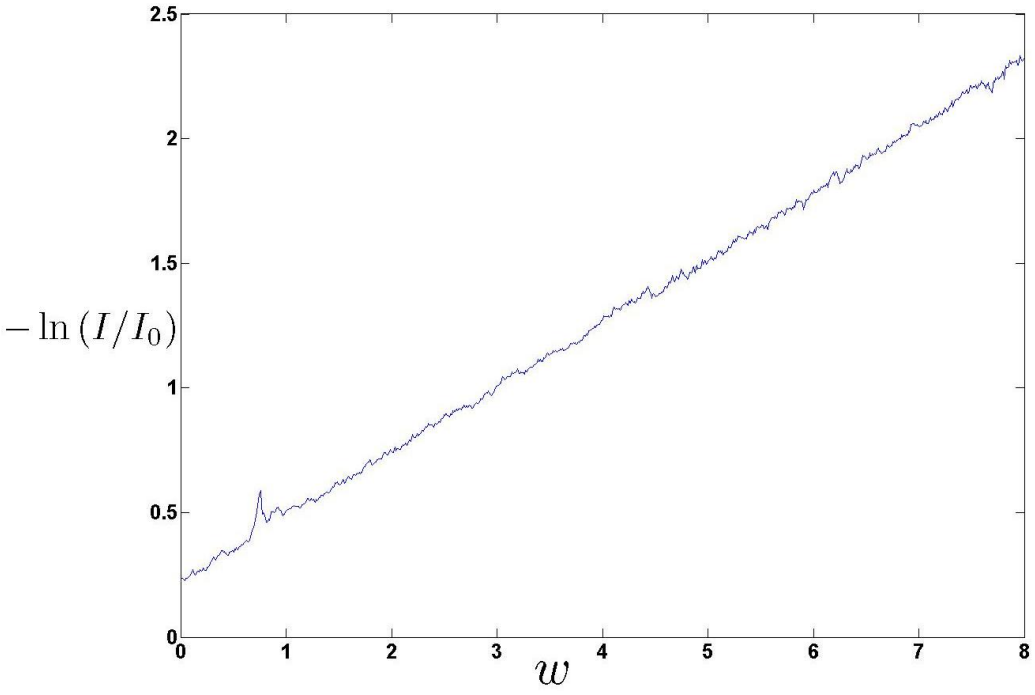

Fig. 14. Absorption of light through a triangular wedge filled with the Nigrosine solute. Since the absorption increases linearly with the width the molar absorbtivity, ϵ is constant.

traveled in the water channel accounting for parallax. The error in mixing fraction $d\overline{f}_1$ is:

$$d\overline{f} = \frac{1}{\epsilon L}\sqrt{\left(d(\epsilon L)\overline{f}\right)^2 + \sum_{n=0}^{N}\left(\frac{1}{N}\frac{dI(t_n)}{I(t_n)}\right)^2 + \left(\frac{dI_0}{I_0}\right)^2} \tag{2.13}$$

$$= \sqrt{\left(\frac{d(\epsilon L)}{\epsilon L}\overline{f}\right)^2 + \frac{1}{N}\left(\frac{1}{\epsilon L}\frac{dI}{I}\right)^2 + \left(\frac{1}{\epsilon L}\frac{dI_0}{I_0}\right)^2} \tag{2.14}$$

To reduce error, the quantity ϵL is set dynamically by observing an area above the splitter plate at the channel entrance where $f = 1$. Similarly, any shift in background intensity is adjusted such that an area below the splitter plate at the channel entrance has $f = 0$. Thus $d(\epsilon L)$ and dI_0 are the average rms of those areas (very small). To

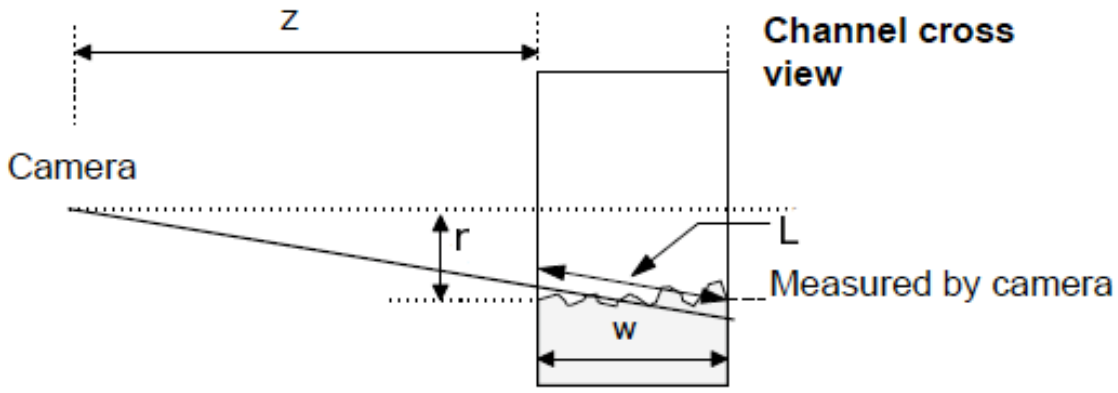

Fig. 15. Parallax error: light travels along distance L, not channel width w, and the distance away from the centerline r has bias depending on how far back the camera is from the channel (z).

measure the uncertainty in the image dI, the wedge is again filled with the Nigrosine solution and placed in the channel. Any variation (rms) of this static (no flow) set of photographs is thus associated with image error dI.

Parallax from a finite sized image (water channel) and a point-like camera has a consequence that the length and angle that the light travels through the channel to the camera depends on the position in the channel, as shown in Figure 15. A channel width of w with the camera a distance z away from the channel, light a distance $r = \sqrt{(x^2 + y^2)}$ away from the centerline gives a different length L. Additionally there is a bias in the position x and y from the parallax as the light collected is not perfectly horizontal nor along a constant streamwise location. Accounting for refraction due to the speed of light in water v_{water} and air v_{air}, this position error δx and δy is:

$$dx = w\frac{v_{water}}{v_{air}}\frac{x}{\sqrt{z^2+x^2\left(1-\left(\frac{v_{water}}{v_{air}}\right)^2\right)}}, \tag{2.15}$$

$$dy = w\frac{v_{water}}{v_{air}}\frac{y}{\sqrt{z^2+y^2\left(1-\left(\frac{v_{water}}{v_{air}}\right)^2\right)}}, \tag{2.16}$$

and the length the light travels in the channel is $L = \sqrt{\delta x^2 + \delta y^2 + w^2}$. The distance from the camera to the channel was 20 feet, resulting in $dx/x \sim dy/y \sim 2.4\%$.

CHAPTER III

RESULTS OF SINGLE MODE INITIAL CONDITIONS

A. Effect of Single-mode Initial Conditions

The effect of single mode initial conditions on the growth rate of the mixing height h are examined using the low-Atwood water channel facility at Texas A&M, as described in the previous section. The experiments performed to examine the effect of single mode perturbations on Rayleigh-Taylor mixing are tabulated in Table II including the amplitude, period, and wavelengths.

Table II. Values of the flapper amplitude A_0 and period T, resulting initial condition wavelength λ, normalized initial condition wavelength $\lambda^\star = \lambda(Ag/\nu^2)^{1/3}$, convective velocity U, and Atwood number A, from densitometer measurement.

Run	A_0 (mm)	T (s)	λ (cm)	$\lambda^\star$	U ($\frac{cm}{s}$)	$A \times 10^{-4}$
1	0	0	0	0	5.71	9.64
2	0.20	0.35	2	46.2	5.71	9.29
3	0.31	0.52	3	69.2	5.71	9.29
4	0.42	0.70	4	92.5	5.71	9.39
5	0.62	1.05	6	147	5.71	12.0
6	0.82	1.40	8	196	5.71	12.0

Sample pictures of the experiment for each case are shown in Figures 16, 17. The applied wavelength in each case grows to be the dominant wavelength, although it is not as evident in the 2 and 3 cm cases since the wavelengths are closer to the natural wavelengths already present in RT mixing. The boundary layer off the flapper is approximately 5 mm per side, resulting in a 1 cm wake off the flapper tip that can be

(a) no-flap

(b) 2 cm wavelength

(c) 3 cm wavelength

Fig. 16. Sample of images from each experiment shown for no-flap, 2 cm, and 3 cm wavelength,(top to bottom).

visually seen in the larger wavelength cases. The classic Rayleigh-Taylor bubbles and spikes are evident, and increasing in size for the larger initial conditions. No leaning or complex interactions from the initial conditions were observed.

(a) 4 cm wavelength

(b) 6 cm wavelength

(c) 8 cm wavelength

Fig. 17. Sample of images from each experiment shown for 4 cm, 6 cm, and 8 cm wavelength,(top to bottom).

The average density $\overline{f}_1$ and uncertainty $d\overline{f}_1$ contours for all cases are similar, shown in Figures 18,19 and 20, 21 respectively. The mixing height versus time is shown in Figure 22, nondimensionalizing time $\tau = ((Ag)^2/\nu)^{1/3}$ and height $\mathcal{H} = h(\nu^2/(Ag))^{1/3}$ with gravity $g = 9.793$ m/s^2, Atwood, A and viscosity $\nu = 7.6 \times 10^{-7}$ m^2/s (water at 33 °C). With this nondimensionalization, the channel height is ~ 395 (depends on Atwood number).

Qualitatively it is observed in Figure 22 that the mixing height $\mathcal{H}$ grows linearly for the large initial conditions case, and slightly quadratically for the no-flap case. A quadratic curve fit for the no-flap case from $5 \leq \tau \leq 20$ is $\mathcal{H} = 5.6 + 2.7\tau + 0.037\tau^2$ with $R^2 = 0.996$, showing a very weak quadratic dependence. The 95% confidence interval on the quadratic term is between 0.033 and 0.043. Using a power law fit yields $\mathcal{H} = 1.6\tau^{1.24} + 8.4$ with $R^2 = 0.996$ and a 95% confidence interval on the exponent between 1.20 and 1.27. Beyond $\tau \approx 20$ the mixing height is $h \approx 0.2H$ and $h \ll H$ is no longer valid. The 2, 3, and 4 cm cases all seem to start with constant velocity, and then leave the common terminal velocity line and approach the slightly quadratic no-flap growth rate. A larger facility would be required to determine if the 6 and 8 cm cases would ultimately follow suit and approach the no-flap case.

The uncertainty $d\mathcal{H} = dh(Ag/\nu^2)^{1/3}$ is shown in Figure 23 and includes by its normalization the uncertainty in Atwood and viscosity. Viscosity is taken from NIST data based on the average temperature of the two channels with an uncertainty based on a 1 degree Centigrade variation (2% relative error). Relative error starts near 15% but tapers down to 5% near $\tau = 15$. This is because there are more pixels to more accurately resolve the location of $\overline{f}_1 = 0.95$. The experimental uncertainty is less than the difference in the curves and so the trend as observed above is evidence of initial condition effects.

The growth parameter α is plotted versus nondimensional time, and is shown to

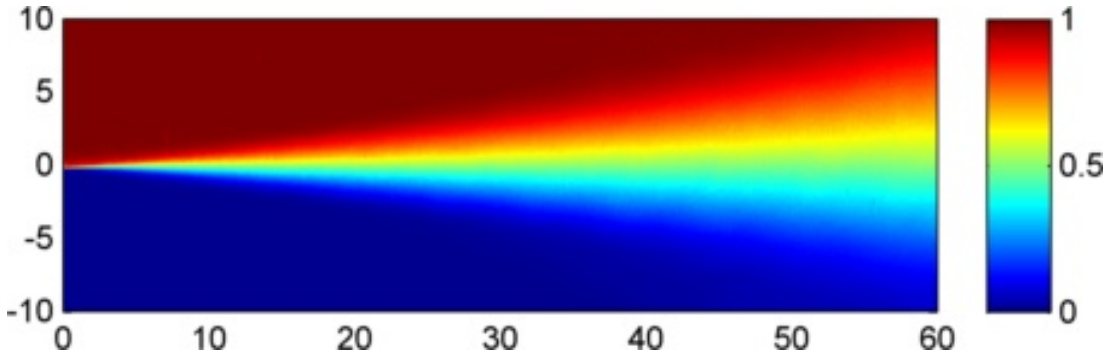

(a) No-flap

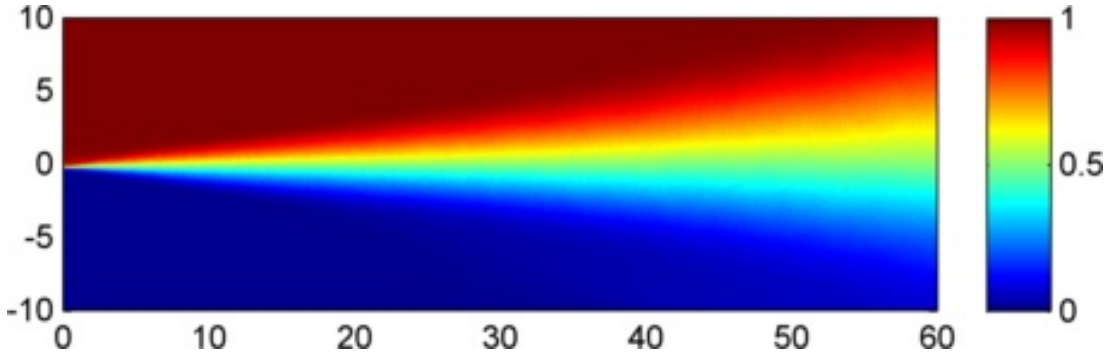

(b) 2 cm wavelength

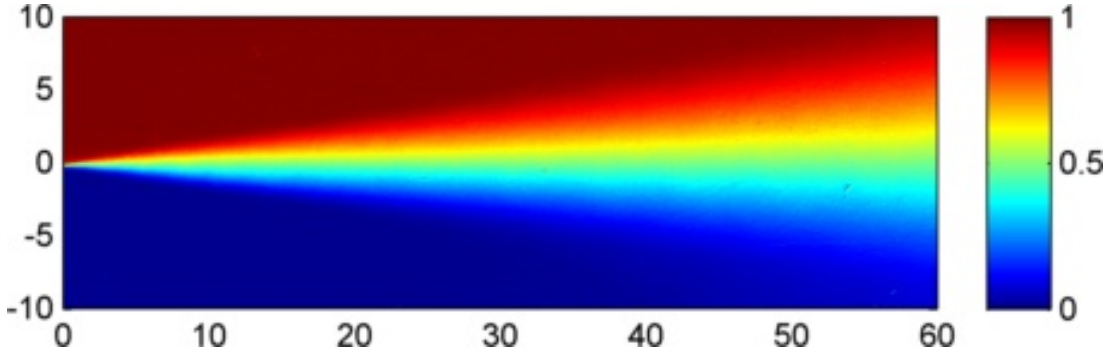

(c) 3 cm wavelength

Fig. 18. Average density $\overline{f}_1$ for the no-flapping, 2 cm, 3 cm cases (top to bottom) as a function of vertical height above the flapper and downstream distance (cm).

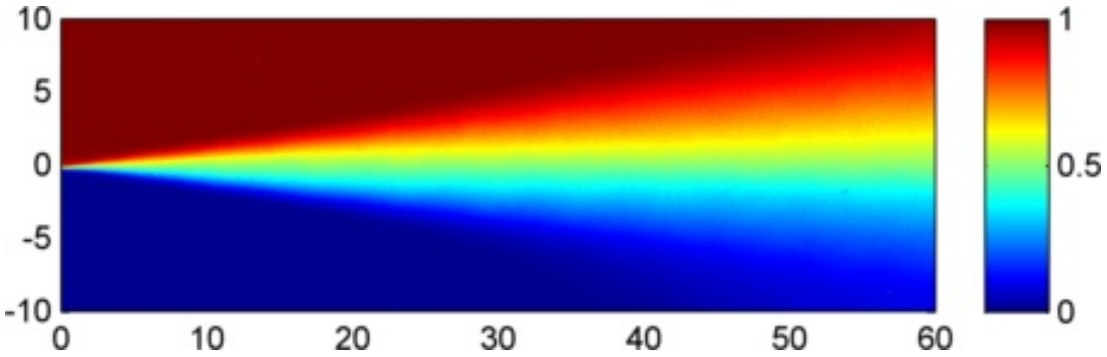

(a) 4 cm wavelength

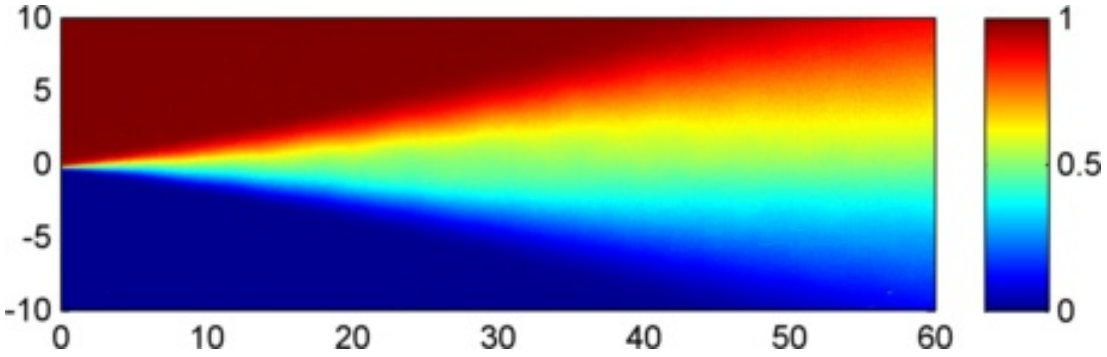

(b) 6 cm wavelength

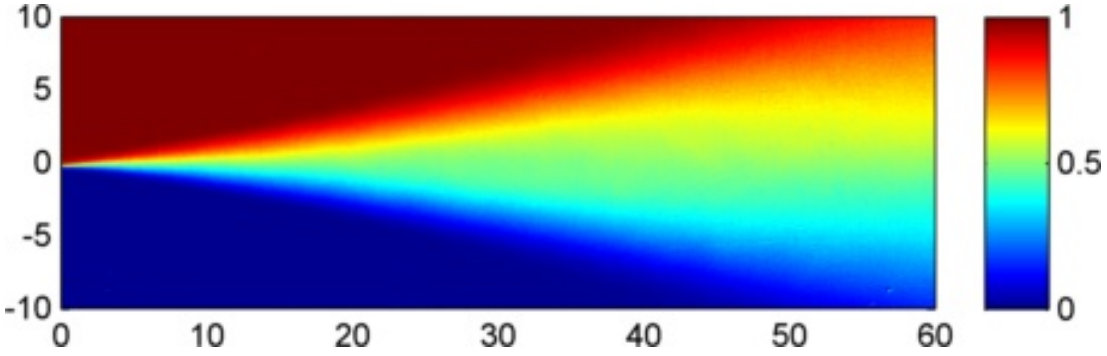

(c) 8 cm wavelength

Fig. 19. Average density $\overline{f}_1$ for the 4 cm, 6 cm, 8 cm cases (top to bottom) as a function of vertical height above the flapper and downstream distance (cm).

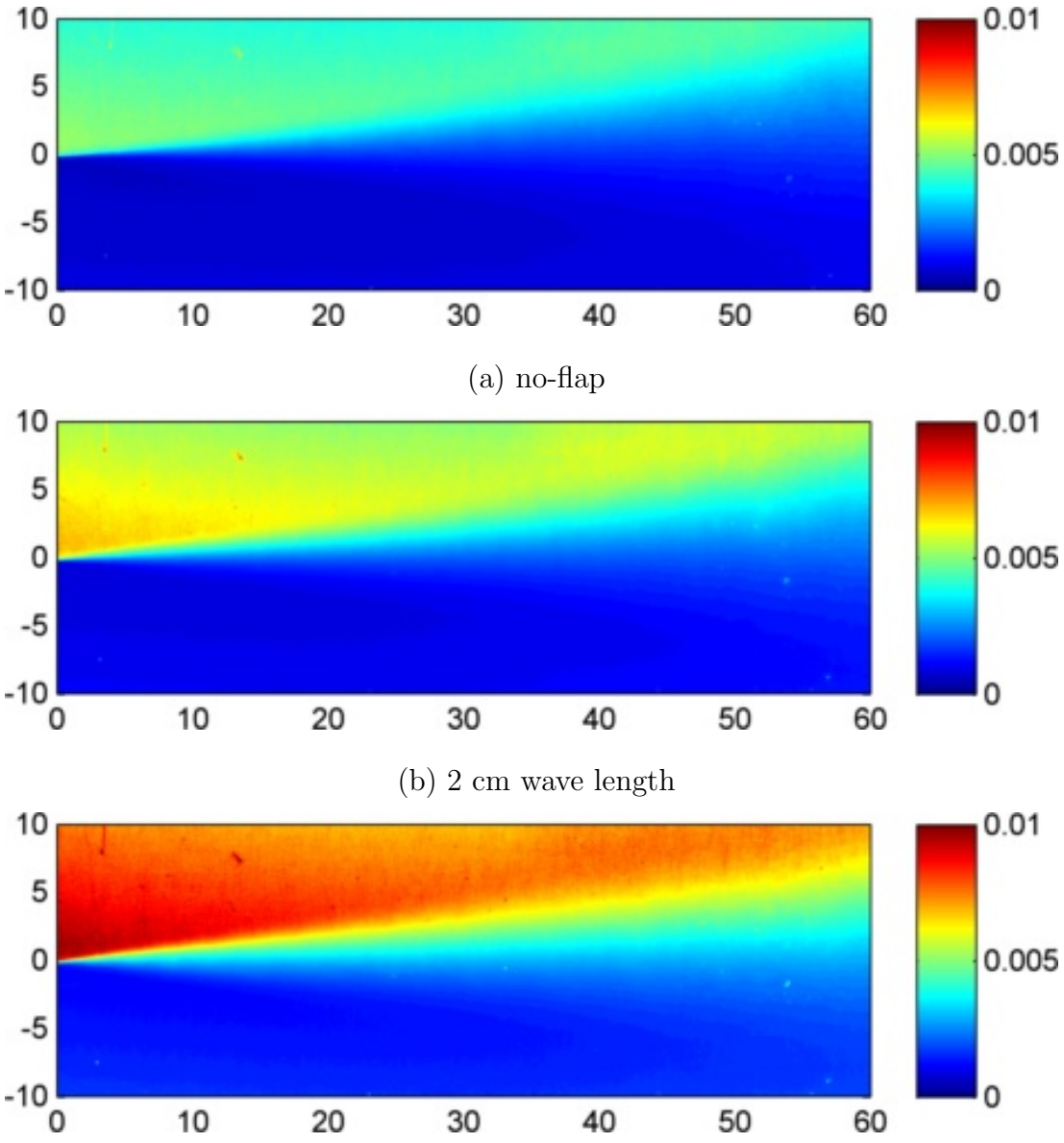

(a) no-flap

(b) 2 cm wave length

(c) 3 cm wave length

Fig. 20. Average density $\overline{f}_1$ uncertainty for the no-flapping, 2 cm,, 3 cm, (top to bottom) cases as a function of vertical height above the flapper and downstream distance (cm).

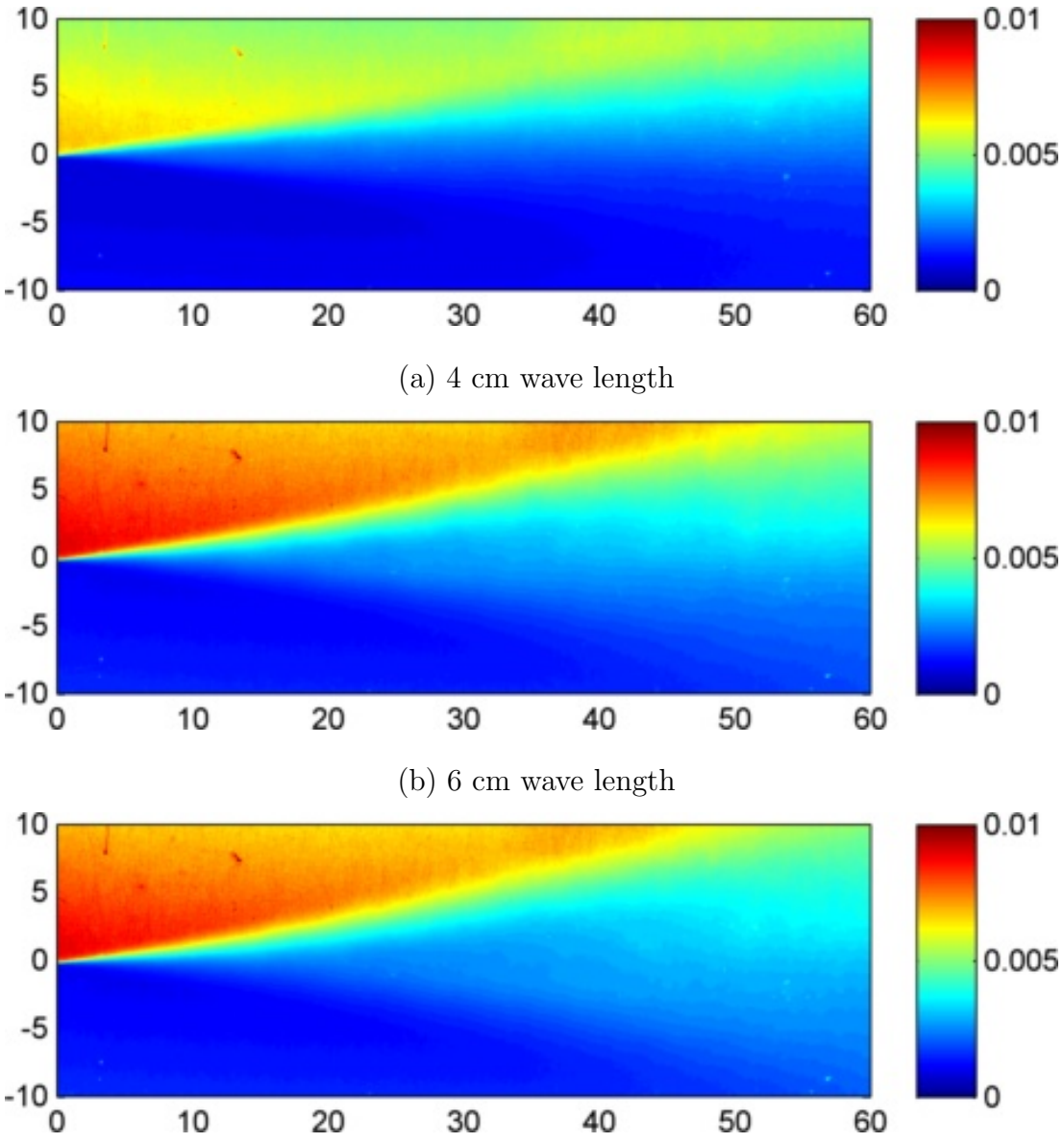

(a) 4 cm wave length

(b) 6 cm wave length

(c) 8 cm wave length

Fig. 21. Average density $\overline{f}_1$ uncertainty for the 4 cm, 6 cm, and 8 cm (top to bottom) cases as a function of vertical height above the flapper and downstream distance (cm).

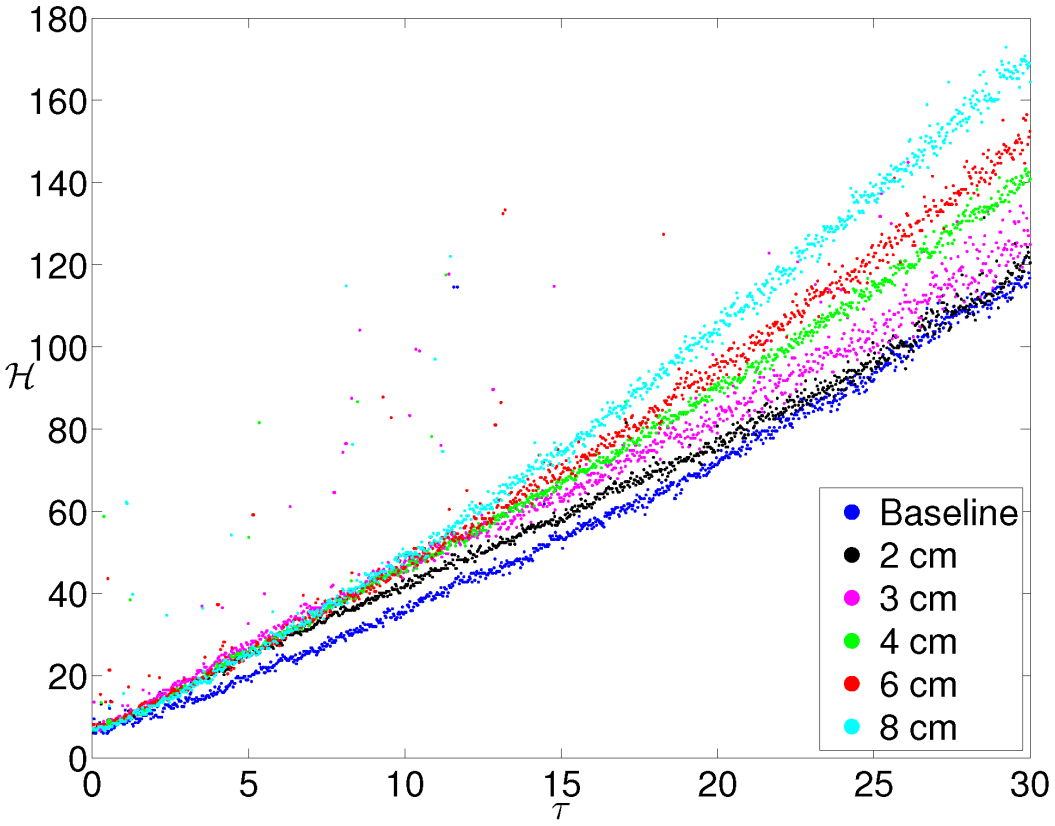

Fig. 22. Mixing height $\mathcal{H} = h(Ag/\nu^2)^{1/3}$ versus time $\tau = t((Ag)^2/\nu)^{1/3}$ for no perturbations and 2, 3, 4, 6, and 8 cm perturbations. The no perturbation case has a slight quadratic dependency. Each of the initial conditions starts on a terminal velocity (straight line) and eventually deviate towards the no perturbation case. The water channel facility is not large enough to determine when or if the 6 and 8 cm perturbations would follow the same trend.

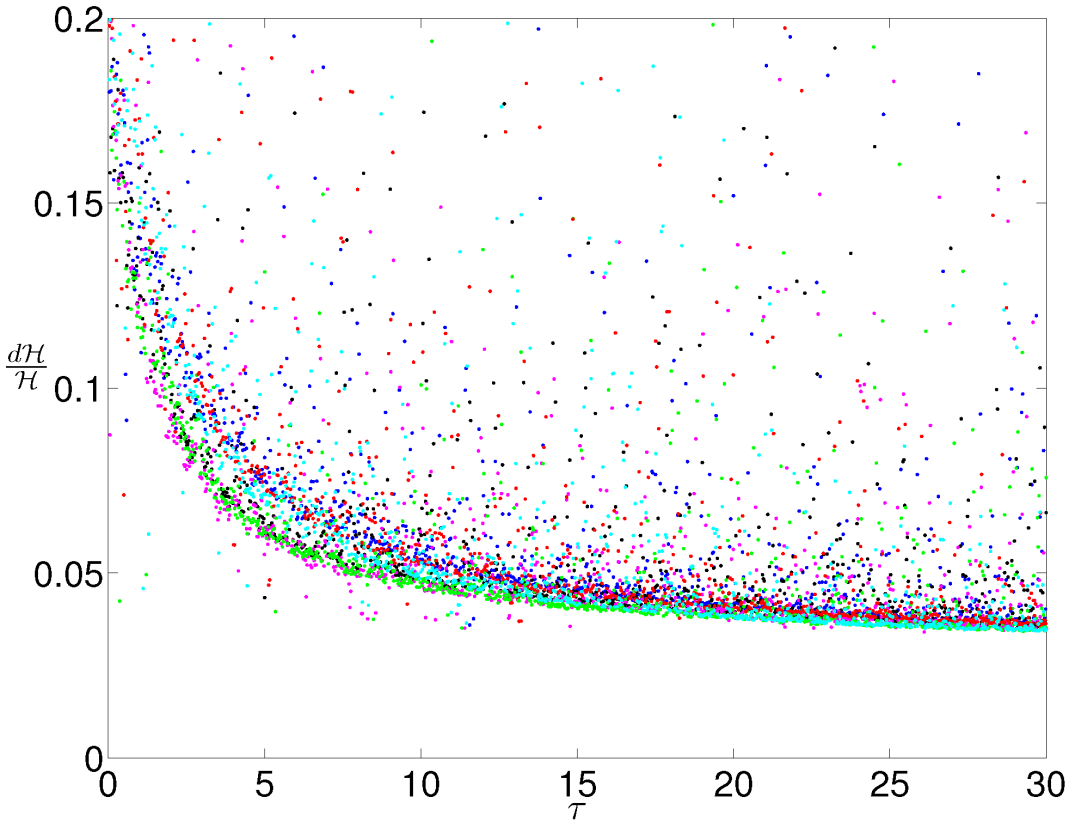

Fig. 23. All cases show the same growth rate within uncertainty. The spikes are due to noise in the system.

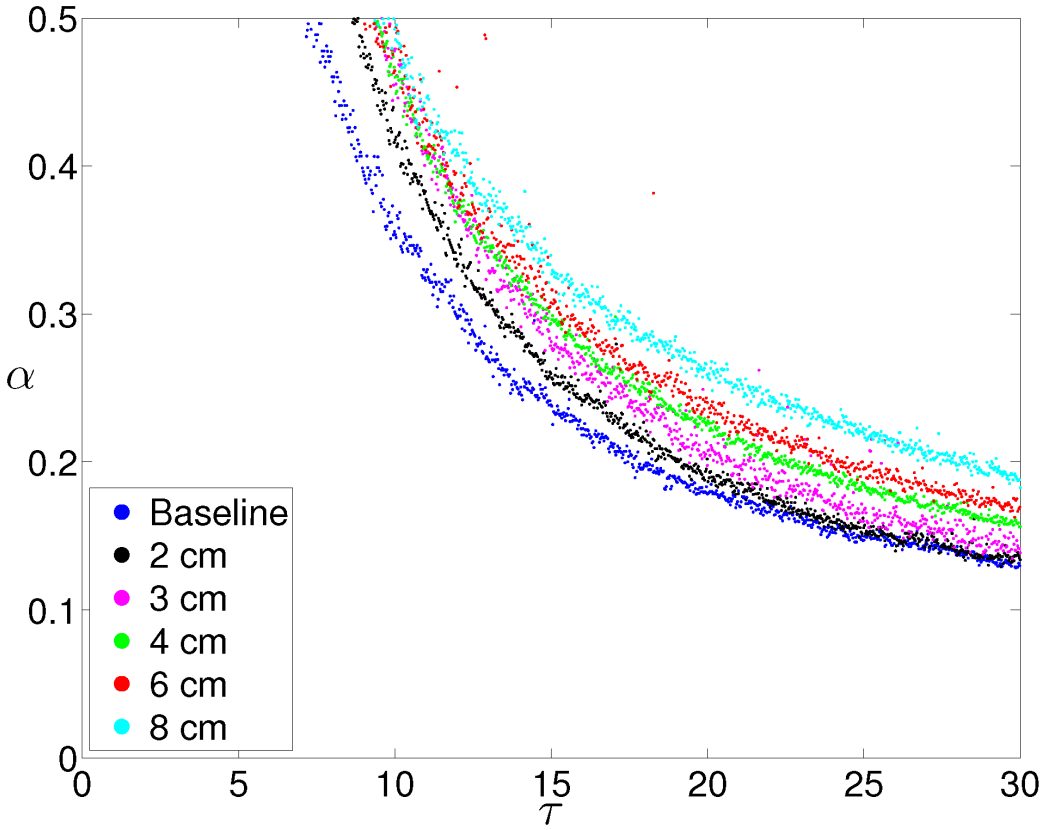

Fig. 24. The growth parameter α vs. nondimensional time. α remains changing, indicating that the third regime has not been reached.

be still changing as shown in Figure 24. The failure of α to asymptote to a value is consistent with other experiments and simulations. Though other researches attempt to establish a consistent value for α, no one has yet done so. This indicates that experiments have yet to arrive and capture data for the third regime of chaos were initial conditions are lost. For this particular experiment, one possible avenue which will likely assist in establishing α as a growth parameter, is to construct a larger channel were data on late time mixing can be acquired.

CHAPTER IV

CONCLUDING REMARKS

After careful analysis of the data it is evident that the single wavelength initial conditions had an effect on the growth rate of the mixing width. However, exactly what is causing the different growth rates is open to interpretation. As discussed in Chapter III, it appears that the 2 cm and 3 cm wavelength approach to the no-flap condition. The 4 cm wave length seems to start asymptotic behavior to the no-flap condition as well, however, the channel's physical domain is too small to determine if that is indeed the case. Similarly, the 6 cm and 8 cm wave length may at later time approach to the no flap condition. As stated in Chapter I, Young assumed that initial conditions are lost, clearly this is not the case as observed in this experiment. However, following the trend of the growth rates it is very likely that at late time when chaos is the dominant regime that initial conditions are indeed lost. Moreover, in this regime the length scale gt^2 describing the growth rates may be adequate. Be that as it may, the current research is primarily interested in early time evolution of RT mixing, and therefore effects of initial conditions are valid as this research showed. This conclusion leads to the result that in early time when the Reynolds number ($Re = \frac{\dot{h}h}{\nu}$) is still sufficiently small, viscous effects can not be excluded from the growth rate nondimensionlization. It can be shown therefore, that

$$\mathcal{H} = h((Ag)/\nu^2)^{1/3} \tag{4.1}$$

is a possible nondimensionlization of the mixing height growth rate.

Additionally, it is observed that the 8 cm wavelength homogenizes the mix faster than the lower wavelength within the mixing width.

1. Remarks On Asymptotic Growth Rates

One question that should be asked is why are the growth rates of the initial conditions regardless of wave length, start with a higher growth rate than the no flap condition? The answer could be quite simple. The energy input by the flapper enables the growth rate to skip over the exponential growth period, thus the growth of the mixing height starts with constant velocity. And so at later time all growth rates approach a single terminal velocity growth rate, which in the case of this experiment is the no-flap condition.

2. Remarks On Experimental Setup

The water channel facility is a novel idea which enables researches to evaluate the RT mixing width growth rates over a long time. The channel is simple to operate and is relatively cheap to maintain. The channel can offer a vast range of experiments, some of which were presented in Chapter I. Additionally, reiterating its simplicity, only one individual is required to perform experiments. However, the channel does present some limitations. It is imperative while conducting experiments, that free-stream turbulence is minimized in the test section. Any possible sources of turbulence in the free-steam will interfere with mixing width growth rates. For this current experiment only when the laminators were installed a few inches up-stream from the flapper, was there no free-stream turbulence observed. However, installing the laminators that close to the test section meant that velocity profiles exiting the laminators were interfering with the growth mixing width. In addition, before each experiment air had to be removed from with in the laminators, a process that required some additional 20 minutes per experiment. However, the complete removal of air could not be confirmed.

3. Future Work

It is recommended that a new test channel be manufactured to replace the original based on the following observations:

- Channel is located in a building that loses power and water supply regularly.
- Channel is 15 years old, is leaking and rusting in many areas.
- Channel should be set on a liftable base so that air can be removed from the underside of splitter plate.
- Channel should be larger in order to achieve higher Re numbers.

These few items should improve the overall performance of the channel, which will permit further research development. For future research there are numerous experiments that can be performed which will help affirm the results that come from the channel. Some possible ideas are:

- Rerun current experiments with salt driven buoyancy, and compare data.
- Run channel with out density gradient to establish a valid base line for the channel, i.e. free-stream turbulence.

This experiment was a great success as it has provided data that can lead to further research implementing multi-mode at the interface. It is the hope that mixing induced by RT hydrodynamic instability should be further understood so that in the future fusion energy could be sustained and thus reduce the dependency for carbon based energy.

REFERENCES

[1] S. Rahmstorf, "The current climate," *Nature*, vol. 421, p. 691, February 2003.

[2] L. Rayleigh, "Investigation of the equilibrium of an incompressible heavy fluid of variable density," *Proc. Lond. Math. Soc.*, vol. 14, pp. 170–177, 1883.

[3] G. Taylor, "The instability of liquid surfaces when accelerated in a direction perpendicular to their planes," *Proc. of the Royal Soc. of London, Series A, Mathematical and Physical Sciences*, vol. 201, pp. 192–196, March 1950.

[4] J. D. Lindl and W. C. Mead, "Two-dimensional simulation of fluid instability in laser-fusion pellets," *Phys. Rev. Lett.*, vol. 34, no. 20, pp. 1273–1276, May 1975.

[5] R. Betti, "Hot spot dynamics and hydrodynamic instabilities," July 2009, presented for the High Energy Density Physics Summer School.

[6] G. Dimonte, D. L. Youngs, A. Dimits, S. Weber, M. Marinak, S. Wunsch, C. Garasi, A. Robinson, M. J. Andrews, P. Ramaprabhu, A. C. Calder, B. Fryxell, J. Biello, L. Dursi, P. MacNeice, K. Olson, P. Ricker, R. Rosner, F. Timmes, H. Tufo, Y.-N. Young, and M. Zingale, "A comparative study of the turbulent Rayleigh–Taylor instability using high-resolution three-dimensional numerical simulations: The Alpha-Group collaboration," *Phys. of Fluids*, vol. 16, no. 5, pp. 1668–1693, 2004.

[7] M. R. Petersen, "Baroclinic vorticity production in protoplanetary disks part ii: Vortex growth and longevity," *The Astrophy. J.*, pp. 192–196, December 2006.

[8] A. Banerjee and M. J. Andrews, "Statistically steady measurements of Rayleigh-Taylor mixing in a gas channel," *Phys. of Fluids*, vol. 18, pp. 192–196, March 2006.

[9] D. L. Youngs, "Numerical simulation of turbulent mixing by Rayleigh-Taylor instability," *Physica D*, vol. 12, pp. 32–44, 1984.

[10] S. Chandrasekhar, *Hydrodynamic and Hydromagnetic Stability.* London: University Press, 1961.

[11] G. Dimonte, P. Ramaprabhu, D. Youngs, M. J. Andrews, and R. Rosner, "Recent advances in the turbulent Rayleigh-Taylor instability," *Phys. Plasmas*, vol. 12, no. 056301, pp. 1–6, 2005.

[12] P. Ramaprabhu, G. Dumonte, and M. J. Andrews, "A numerical study of the influence of initial perturbations on the turbulent Rayleigh-Taylor instability," *J. Fluid Mech.*, vol. 536, no. 1, pp. 285–319, 2005.

[13] D. H. Olson and J. W. Jacobs, "Experimental study of Rayleigh–Taylor instability with a complex initial perturbation," *Phys. Fluids*, vol. 21, no. 3, pp. 034–103, 2009.

[14] K. Read, "Experimental investigation of turbulent mixing by Rayleigh-Taylor instability," *Physica D: Nonlinear Phenomena*, vol. 12, pp. 45–58, July 1984.

[15] D. B. S. M. J. Andrews, "A simple experiment to investigate two-dimensional mixing by RayleighTaylor instability," *Phys. of Fluids*, vol. 2, pp. 922–927, June 1990.

[16] G. Dimonte and M. Schneider, "Turbulent Rayleigh-Taylor instability experiments with variable acceleration," *Phys. Rev. E*, vol. 54, no. 4, pp. 3740–3743, Oct 1996.

[17] A. Snider, "Rayleigh Taylor and shear driven mixing with an unstable thermal stratification," *Phys. of Fluids*, vol. 6, pp. 3324–3334, October 1994.

[18] K. Leicht, "Effects of initial conditions on Rayleigh Taylor mixing development," Master's thesis, Texas A&M University, College Station, TX, May 1997.

[19] H. Schlichting and K. Gersten, *Boundary Layer Theory.* Springer, 2000.

APPENDIX A

SUMMARY OF CHANGES

In summary, the improvements, modifications, and upgrades to the low-Atwood water channel facility, the experimental procedures, and data analysis are:

- Atwood number by densitometer measurement (20% error reduction).
- Use local gravity of 9.793 m/s^2 (2% error reduction).
- Optical instead of hand/eye based velocity measurements.
- More appropriate estimation for mean convective velocity.
- Installation of servo-motor controlled flapper (deliverable).
- Reduction of system vibrations by disconnecting and suspending inlet pipes.
- Free-stream turbulence to zero, resulting in big boundary layer.
- Adding free-stream turbulence to system to reduce boundary layer size.
- Optics upgrade (two orders of magnitude reduction in error).
  - Professional digital SLR camera with high quality lenses.
  - Flashes with less than 1 sec. recharge rate.
  - White diffuse reflective sheet for uniform background.
  - Black absorptive shroud for eliminating reflections.
- Linear absorptivity across channel width (instead of half-width).
- Optics uncertainty analysis updated:
  - Parallax uncertainty added.
  - Refraction of light in water added.

  - Optics r.m.s. instead of turbulence r.m.s. used for error.
  - Uncertainty of absorptivity added.
  - Uncertainty of channel width added.

- Dynamically accounting for variation in total absorption in addition to any dynamical changes in background intensity.
- Uncertainty propagated to mixing height (not equal to density error).

APPENDIX B

REYNOLDS AVERAGED NAVIER-STOKES ANALYSIS

The mean transport of scalar f by a mean velocity U is modeled by the transport equations:

$$U\frac{\partial f}{\partial x} = \Gamma\left(\frac{\partial^2 f}{\partial x^2} + \frac{\partial^2 f}{\partial y^2}\right) \tag{B.1}$$

including molecular and turbulent diffusion Γ. In the water channel, this is mathematically parabolic if upstream does not affect downstream, or:

$$\frac{\partial^2 f}{\partial y^2} \gg \frac{\partial^2 f}{\partial x^2} = \frac{1}{U^2}\frac{\partial^2 f}{\partial t^2} \tag{B.2}$$

where Taylor's frozen turbulence $x = Ut$ is invoked.

Assuming a cubic representation of f where $f = 1$ at $y = h$, $f = 0$ at $y = -h$, $f = 0.5$ at $y = 0$, and h being the height of the mixing layer at a position x.

$$f = -\frac{1}{4}\left(\frac{y}{h}\right)^3 + \frac{3}{4}\left(\frac{y}{h}\right) + \frac{1}{2} \tag{B.3}$$

Assuming that $h = \alpha A g t^2$ yields after some algebra:

$$U^2 \gg 7\frac{y^2}{t^2} - 6(\alpha A g t)^2 \tag{B.4}$$

This criterion is maximized when $y = h = \alpha A g t^2$:

$$U^2 \gg (\alpha A g t)^2 = \frac{1}{4}\left(\frac{\partial h}{\partial t}\right)^2 = \frac{1}{4}\left(\frac{\partial h}{\partial x}U\right)^2 \tag{B.5}$$

$$\left(\frac{\partial h}{\partial x}\right)^2 \ll 4 \tag{B.6}$$

Assuming $\ll$ to be two orders of magnitude:

$$\frac{\partial h}{\partial x} = 0.2 = 2\alpha A g x / U^2 \tag{B.7}$$

the furthest distance downstream $x = U\sqrt{D/(\alpha A g)}$ where D is the largest mixing layer size, which is 4 inches based on the current channel design.

$$U = 10\sqrt{D\alpha A g} \tag{B.8}$$

Assuming a large value of alpha (for uncertainty reasons) of $\alpha \sim 0.07$, $D = 4$ inches:

$$U = 264\frac{\text{cm}}{\text{s}}\sqrt{A} \tag{B.9}$$

For A=0.0007 (5 Celsius temperature difference), this is 7 cm/s. For A = 0.002 (13.5 Celsius difference), this is 11.8 cm/s.

APPENDIX C

EXPERIMENTAL PROCEDURES

The current experimental procedure as described here is based the operation of one individual. All steps are described in chronological order of operation, any deviation may cause the experiment to require longer preparation time.

Basic experimental Procedure

1. Begin filling tanks with water.
   (a) Place the water hose in “hot tank” in begin filling.
   (b) Align valves such that the piped water only enters “cold tank”, and begin filling.
2. Close all drain valves at the channel exit plenum.
3. Setup motor servo control.
   (a) Place motor servo and power source along side channel at appropriate location.
   (b) Connect computer with CAT 5 cable to servo.
   (c) Connect servo to motor (two cables).
   (d) Using your hand physically move flapper to ensure ease of movement.
   (e) Connect servo power source to 115 v outlet.
   (f) Using your hand verify that motor does not move freely.
   (g) Ensure IP address in the computer matches servo IP address.

(h) Servo IP: 166.091.148.10, 2nd line: 255.255.254.0, 3rd line:165.091.148.1

(i) Open Galil tolls software.

(j) In the GUI click the blue + sign icon.

(k) Ensure the key board is set to caps.

(l) In the command line, type PR100, the motor should move slightly in the clockwise direction.

(m) Continue moving motor until flapper is lined up with horizontal marking on channel wall.

(n) Recall that the motor has 4000 counts per revolution.

(o) Type DP0(DP Zero), this will indicate to the servo that current position is home.

(p) Verify by typing PA?, answer should be zero.

(q) Click the wrench icon to run auto tune, and set gains.

(r) After auto tune has completed, attempt to run program by clicking the down second down arrow icon, while feeling the fly wheel on the motor.

(s) Motor should operate smoothly through cycle.

(t) Adjust gains until excused program runs smoothly.

(u) Rerun steps I through P.

4. ALL PUMPS SHOULD ONLY BE TURNED OFF AND ON USING ELECTRIC SWITCH ON OUTLET.

5. After water level in "hot tank" has reached $\frac{1}{3}$, turn on sump pump.

6. Permit the tanks to fill to marked level on tank.

7. Adjust hot and cold valves such that water temperature in hot tank is $\sim 5^{\circ}$ c above cold water tank.
8. Fill water channel using water hose.
9. Set up camera.
   (a) Set camera on tripod at a distance of 240 inches from test section.
   (b) Level camera.
   (c) Set camera F-stop to 16, and aperture to 320.
   (d) Zoom in to maximum.
   (e) Place 24 inch ruler inside test section on top of 5 inch spacer.
   (f) Slightly press capture button to focus camera on ruler.
   (g) Set focus to manual on zoom lance.
   (h) Set camera to raw image file format.
   (i) Take one picture of the Ruler.
10. Set tarp shroud between channel and camera.
11. Mix 5 grams of Nigrosine powder in cold water tank.
12. Fill wedge with cold tank water, and place it inside channel.
13. Take 100 pictures of wedge.
14. Remove wedge, and take 100 pictures of channel.
15. Secure sump pumps check water temperature, take water samples for density measurements.
16. Plug in main pumps and open channel drain valves.

VITA

Yuval was born in Israel in 1972, and moved with his family to the US in 1985. In 1991, Yuval started his career in the US Navy serving aboard the USS MT Vernon as a propulsion Engineer, and later on the USS Shasta as Electro Hydraulic Winch specialist. After 6 years of service Yuval joined Domatex the family business in Houston Texas. Domatex specializes in steel fabrication of unique trailers and containers. In 2000, Yuval started college at UT Austin in Mechanical Engineering. Yuval worked at the Fluid's Lab, and under the supervision of Dr. Schmidt developed a unique apparatus for the visualization of developing flow in a pipe, transient flow from laminar to turbulent, and pressure drop in a pipe. In addition, Yuval served as a Fluids Lab instructor under the supervision of Dr. Bogard. Prior to completing his degree however, Yuval had to return to Domatex in order to work on some pressing matters. In 2005, Yuval introduced Solidworks as a design and engineering tool to the everyday fabrication process. Cosmos was used extensively in the design of unique heavy Duty trailers that haul up to 120,000 LBS of load. In 2008 Yuval earned his Bachelor degree from University of Texas at Austin. He began his masters program in the Mechanical Engineering Department at Texas A&M University in August of 2008, and joined the Fluids, Turbulence and Fundamental Transport Lab (FT2L) under Dr. Andrew Duggleby. He graduated in December 2009.

He may be reached at:

Yuval Doron
c/o Dr. Andrew Duggleby
Department of Mechanical Engineering
Texas A&M University
College Station, TX 77843-3123